

# Marangoni instability in a viscoelastic binary film with cross-diffusive effect

Rajkumar Sarma<sup>1</sup> and Pranab Kumar Mondal<sup>1,†</sup>

<sup>1</sup>Department of Mechanical Engineering, Indian Institute of Technology Guwahati, Guwahati, Assam 781039, India

(Received 13 January 2020; revised 9 August 2020; accepted 26 October 2020)

Viscoelastic liquids are usually blends of a polymeric solute and a Newtonian solvent. In the presence of a temperature gradient, stratification of these solutes can take place via the Soret effect. Here, we investigate the classical Marangoni instability problem for a thin viscoelastic film considering this binary aspect of the liquid. The film, bounded above by a deformable free surface, is subjected to heating from below by a solid substrate. Linear stability analysis performed numerically for perturbations of finite wavelength (short-wave perturbations) reveals that both monotonic and oscillatory instabilities can emerge in this system. In the presence of Soret diffusion, the interaction between thermocapillary and solutocapillary forces is found to give rise to two different oscillatory instabilities, of which one mode was overlooked previously, even for the Newtonian binary mixtures. As a principal result of this work, we provide a complete picture of the susceptibility to different instability modes based on model parameter values. Finally, an approximate model is developed under the framework of long-wave analysis, which can qualitatively depict the stability behaviour of the system without numerically solving the problem.

**Key words:** Marangoni convection, thin films, viscoelasticity

---

## 1. Introduction

A gradient of surface tension caused by inhomogeneities in temperature (thermocapillarity) or concentration (solutocapillarity) on the free surface of a pure liquid or liquid mixtures has the ability to induce motion in its bulk phase. Typically known as the Marangoni convection, this phenomenon is frequently encountered in small-scale systems (e.g. a thin liquid film, droplet, vapour bubble or liquid bridge) where the surface effects dominate over the volumetric ones. Understanding the dynamics of Marangoni convection is essential for optimizing operations such as interfacial heat and mass transport (applications include thin-film evaporation, liquid–liquid extraction) and materials processing problems (semiconductor crystal growth, weld deposition), especially for a microgravity environment where the buoyancy-driven Rayleigh–Bénard convection gets inhibited.

Since the founding experiments of Bénard (1901), several theoretical, experimental and numerical investigations have been carried out over the years to elucidate the major features of this convection phenomenon. For a short historical account on these works, the

† Email address for correspondence: [mail2pranab@gmail.com](mailto:mail2pranab@gmail.com)

reader is referred to monographs and review papers by Oron, Davis & Bankoff (1997), Colinet, Legros & Velarde (2001), Nepomnyashchy (2001), Schatz & Neitzel (2001), Craster & Matar (2009) and Shklyaev & Nepomnyashchy (2017). It is now well known that, unlike pure liquids, Marangoni convection in a multicomponent liquid film can develop under the simultaneous actions of thermocapillary and solutocapillary effects. Such liquid mixtures usually exhibit a strong Soret effect (a cross-diffusive effect that leads to the spontaneous generation of solute concentration gradient under an imposed temperature gradient). Therefore, two different physical situations are possible while investigating the Marangoni convection in a multicomponent liquid film: (i) the temperature and the concentration gradients are caused by independent sources (often called double-diffusive convection); and (ii) the temperature gradient is externally imposed, while the Soret effect generates the concentration gradient.

Motivated by their importance in materials processing, and species separation in food, chemistry and biomedical applications, both the aforementioned cases have been extensively investigated in the literature. The double-diffusive problem was pioneered by McTaggart (1983) to analyse the linear stability characteristics of a horizontally infinite binary liquid film. Later, Ho & Chang (1988) extended her analysis to study the nonlinear aspect of the convection process; Arafune, Yamamoto & Hirata (2001) investigated the double-diffusive problem experimentally, while Chen, Li & Zhan (2010) tackled the problem for a confined cavity. More recently, D'Alessio *et al.* (2020) have theoretically analysed the double-diffusive instabilities in a liquid film falling down a heated inclined plate. These analyses demonstrate that both monotonic and oscillatory instabilities are possible in a binary liquid film. The monotonic mode appears when the shear stresses induced by thermal and solutal components enhance each other, and the oscillatory convection develops whenever they counteract.

The cross-diffusive Marangoni convection problem has also been the subject of numerous investigations, starting with the precursor works of Bhattacharjee (1994), Joo (1995) and Skarda, Jacqmin & McCaughan (1998). These authors addressed the problem for a horizontal liquid film resting on an ideally thermally conductive substrate (i.e. considering a constant-temperature bottom boundary condition). Under the framework of linear stability analysis, it was shown that, although monotonic disturbances can emerge in the long-wave form in a non-deformable surface, nevertheless, the free surface deformability is essential for the appearance of long-wave oscillatory perturbations. For a poorly conductive substrate (i.e. the condition of fixed heat flux at the bottom boundary), later Oron & Nepomnyashchy (2004) detected a different kind of long-wave oscillatory disturbance that can develop even without surface deformations. Shklyaev, Nepomnyashchy & Oron (2009) extended this analysis to decipher the short-wave mode of this particular oscillatory instability. Recent research in the field of cross-diffusive Marangoni convection has focused on exploring the role of free surface deformability (Podolny, Oron & Nepomnyashchy 2005; Hu *et al.* 2008; Besthorn & Borcia 2010), the effect of surfactant adsorption/desorption on the free surface (Shklyaev & Nepomnyashchy 2013) or the influence of modulated boundary conditions (Fayzrakhmanova, Shklyaev & Nepomnyashchy 2013) on the stability behaviour of the system. However, it should be noted that all these above-mentioned studies deal with a Newtonian binary mixture.

Despite such remarkable advancements towards understanding the Marangoni convection in Newtonian fluids, relatively little attention has been devoted to viscoelastic liquids. Viscoelastic liquids, e.g. polymeric solutions, biofluids, paints, lubricants, etc., exhibit complex rheological behaviour due to both the viscous and elastic character (Bird, Armstrong & Hassager 1987). A non-trivial relaxation time (a measure of elasticity of the

liquid) significantly alters the dynamics of such liquids from their Newtonian counterpart. Marangoni convection is often encountered in viscoelastic fluids during phenomena such as the drying of thin polymeric films, paint films, etc. (Toussaint *et al.* 2008; Bassou & Rharbi 2009; Bormashenko *et al.* 2010). The convective patterns developed in such liquid films have promising properties for nanotechnological applications, e.g. organic photovoltaics and photodiodes (Heriot & Jones 2005). It is important to note that viscoelastic liquids are usually composed of a polymeric solute and a Newtonian solvent, and thus essentially they are binary mixtures. The Soret effect can yield a stratification of the solutes in such liquids as well (de Gans *et al.* 2003). Usually, while the solutes tend to migrate towards a colder region (owing to their large masses), nevertheless, sometimes, depending on the solvent quality and the temperature of the mixture, they can also move into the warmer region (Zhang & Müller-Plathe 2006; Würger 2007). Such migration of solutes can lead to the development of solutocapillary stress on the free surface of a viscoelastic liquid film. This aspect necessitates the consideration of a complete thermosolutal model to investigate the Marangoni instability problem in a viscoelastic liquid.

In the previously reported studies on Marangoni instability in a viscoelastic film, either this binary aspect of the liquid was completely ignored, or the problem was analysed separately for the thermal and solutal convections (i.e. without considering a complete thermosolutal model). A purely thermal model (Getachew & Rosenblat 1985; Dauby *et al.* 1993; Parmentier, Lebon & Regnier 2000; Sarma & Mondal 2019) suggests the emergence of both monotonic and oscillatory disturbances in the system. The monotonic mode is found to become dominant in a weakly viscoelastic liquid, while the oscillatory instability prevails in highly viscoelastic liquids. However, such a model is inadequate to illustrate the instability modes caused by the solutocapillary force. The solutal problem was analysed by Doumenc *et al.* (2013) and Yiantsios *et al.* (2015) in the context of evaporation in a polymeric film. In these works, the concentration gradient was considered to be solely caused by the difference in evaporation rate between the constituents, neglecting the Soret effect. These analyses provide a deep insight into the problem regarding the onset of convection in the film and the evolution of disturbances in the nonlinear regimes. However, the role of liquid elasticity on the film dynamics is not clear from these works, since the polymeric solution was treated as a Newtonian liquid. Furthermore, it also needs to be pointed out that separate thermal and solutal models are incapable of depicting the instability modes that may emerge from the interaction between them.

The present work aims at developing a complete thermosolutal model to investigate the Marangoni instability problem for a thin viscoelastic film. The liquids considered here can spontaneously generate a concentration gradient via the Soret effect on the imposition of a temperature gradient, e.g. poly(ethylene oxide)/water, poly(vinyl alcohol)/water, polystyrene/dioctyl phthalate (Zhang & Müller-Plathe 2006). Employing a viscoelastic constitutive model to depict the rheology of the liquid, we study the stability characteristics of the system under the framework of linear analysis. Besides exploring the role of liquid elasticity on the underlying convection, the present investigation also reveals the instability modes originating from the interaction between thermocapillary and solutocapillary forces. In light of the results obtained in this work, another principal goal of this paper is to encourage future work with viscoelastic liquids.

The remainder of the paper proceeds as follows. In § 2, we formulate the problem by presenting the set of governing equations and boundary conditions. Linear stability analysis of the system is then carried out in § 3. The stability picture generated by numerically solving the eigenvalue problem is analysed in § 4. In § 5, we study the effect

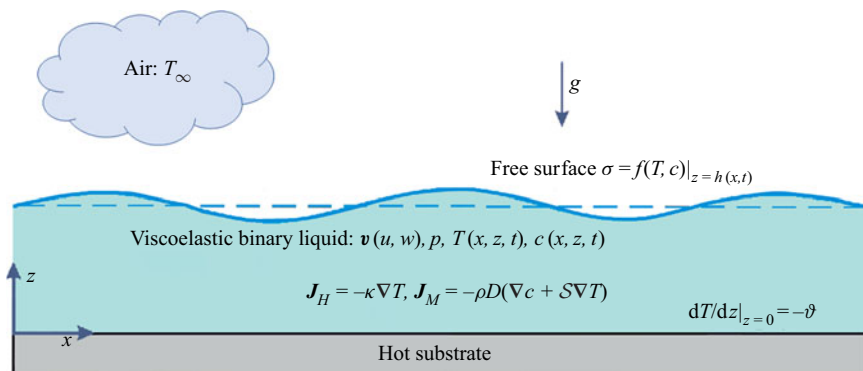


FIGURE 1. Schematic illustration of the physical system under consideration. A thin viscoelastic film (composed of a polymeric solute in a Newtonian solvent), confined between its deformable free surface  $z = h(x, t)$  and a horizontal substrate in the gravitational field  $\mathbf{g}$ , is subjected to a vertical temperature gradient. This applied temperature gradient induces a concentration gradient in the film via the Soret effect. The surface tension gradient arising from inhomogeneities in temperature and concentration at the air–liquid interface induces Marangoni convection in the liquid layer. The dashed line corresponds to the undeformed interface in the quiescent base state.

of liquid elasticity on the spatial structure of eigenvectors at the neutral stability boundary. An approximate model is then developed in § 6. To provide a comprehensive picture of the susceptibility to different instability modes based on model parameter values, we plot the phase diagrams in § 7. And, finally, conclusions are drawn in § 8.

## 2. Mathematical model

### 2.1. Problem statement and the governing equations

We begin by considering a thin, two-dimensional layer of an incompressible viscoelastic polymer solution in the gravitational field  $\mathbf{g}$  (see figure 1). The solution is a binary mixture of polymeric solute and Newtonian solvent, characterized by the relaxation time  $\lambda$ , viscosity  $\mu_o$ , density  $\rho$ , thermal conductivity  $\kappa$ , thermal diffusivity  $\alpha$ , mass diffusivity  $D$  and surface tension  $\sigma$ .

We consider the film to be of infinite horizontal extent  $x \in (-\infty, \infty)$  with unperturbed thickness  $H$ . At the  $z = 0$  plane, the film is in thermal contact with a poorly conductive rigid substrate, while a deformable free surface located at  $z = h(x, t)$  separates it from the ambient gas phase. A transverse temperature gradient exists in the entire binary mixture, which is specified to be  $-\vartheta$  at  $z = 0$ . This signifies that  $\vartheta > 0$  ( $\vartheta < 0$ ) corresponds to the case of heating the liquid layer from the substrate (gas) side. The incorporation of the Soret effect into the analysis indicates that mass flux in the flow domain is a combination of concentration and temperature gradients (de Groot & Mazur 2011). Hence, the heat  $\mathbf{J}_H$  and mass  $\mathbf{J}_M$  fluxes within the film are governed by

$$\mathbf{J}_H = -\kappa \nabla T \quad (2.1a)$$

and

$$\mathbf{J}_M = -\rho D(\nabla c + \mathcal{S} \nabla T), \quad (2.1b)$$

where  $\mathcal{S}$  is the Soret coefficient of the mixture. For a polymeric solution,  $\mathcal{S}$  can be either positive or negative depending on the solvent quality, the mole fractions of the

components and the temperature of the binary mixture (Zhang & Müller-Plathe 2006). A negative (positive) sign of  $\mathcal{S}$  signifies the migration of polymeric solutes towards the warmer (colder) region. It follows from (2.1) that, at the conductive state, the externally applied heat flux generates a temperature difference  $\Delta T = \vartheta H$ , which, in turn, yields a concentration difference  $\Delta c = -\mathcal{S}\Delta T$  across the layer.

Now, above a particular temperature gradient, the thermo- and solutocapillary effects induce Marangoni convection in this mixture. The buoyancy effect is neglected in this study considering the small thickness of the film ( $H \lesssim O(1)$  cm; see Pearson 1958). We assume the surface tension to vary linearly with temperature and solute concentration, dictated by the relationship

$$\sigma = \sigma_o - \sigma_T(T - T_o) + \sigma_c(c - c_o), \quad (2.2)$$

where  $\sigma_o$  is the surface tension at the reference temperature  $T_o$  and concentration  $c_o$ ; and  $\sigma_T = -\partial\sigma/\partial T$  and  $\sigma_c = \partial\sigma/\partial c$  quantify the rate of change of surface tension with respect to temperature and concentration, respectively. It should be noted that for most polymeric solutions  $(\sigma_T, \sigma_c) > 0$  (Doumenc *et al.* 2013). Furthermore, except for  $\sigma$ , all other thermophysical properties are assumed to remain invariant with temperature in this analysis.

In the presence of a linear Soret effect, the equations governing the fields of liquid velocity  $\mathbf{v} \equiv \{u(x, z, t), w(x, z, t)\}$ , pressure  $p(x, z, t)$ , temperature  $T(x, z, t)$  and concentration  $c(x, z, t)$  in the bulk of the film are given by

$$\nabla \cdot \mathbf{v} = 0, \quad (2.3a)$$

$$\rho \left( \frac{\partial \mathbf{v}}{\partial t} + \mathbf{v} \cdot \nabla \mathbf{v} \right) = -\nabla p + \nabla \cdot \boldsymbol{\tau} - \rho g \mathbf{k}, \quad (2.3b)$$

$$\frac{\partial T}{\partial t} + \mathbf{v} \cdot \nabla T = \alpha \nabla^2 T, \quad (2.3c)$$

$$\frac{\partial c}{\partial t} + \mathbf{v} \cdot \nabla c = D \nabla^2 c + \mathcal{S} D \nabla^2 T, \quad (2.3d)$$

respectively, where  $t$  represents time,  $\boldsymbol{\tau} = \begin{bmatrix} \tau_{xx} & \tau_{xz} \\ \tau_{zx} & \tau_{zz} \end{bmatrix}$  is the deviatoric stress tensor,  $\mathbf{k}$  is the unit vector in the  $z$ -direction and  $\nabla \equiv \{\partial/\partial x, \partial/\partial z\}$ . The above set of governing equations are accompanied by the following boundary conditions.

At the  $z = 0$  plane, where the film is in thermal contact with a rigid substrate, the pertinent boundary conditions encompass the no-slip, no-penetration condition for velocity, a specified uniform normal heat flux and the mass impermeability condition, represent respectively by

$$\mathbf{v} = 0, \quad \frac{\partial T}{\partial z} = -\vartheta, \quad \frac{\partial c}{\partial z} = \mathcal{S}\vartheta \quad \text{at } z = 0. \quad (2.4a-c)$$

At the deformable free surface  $z = h(x, t)$ , the boundary conditions comprise the kinematic boundary condition, heat exchange with the ambient gas phase (characterized by Newton's law of cooling), mass impermeability condition and the balance of tangential

and normal stress components, represented respectively by

$$w = \frac{\partial h}{\partial t} + u \frac{\partial h}{\partial x}, \quad (2.5a)$$

$$-\kappa \left( \frac{\partial h}{\partial x} \frac{\partial T}{\partial x} - \frac{\partial T}{\partial z} \right) + q(T - T_\infty) \sqrt{1 + (\partial h / \partial x)^2} = 0, \quad (2.5b)$$

$$\kappa \left( -\frac{\partial h}{\partial x} \frac{\partial c}{\partial x} + \frac{\partial c}{\partial z} \right) - \mathcal{S}q(T - T_\infty) \sqrt{1 + (\partial h / \partial x)^2} = 0, \quad (2.5c)$$

$$\frac{1}{\sqrt{1 + (\partial h / \partial x)^2}} \left\{ \tau_{xz} \left[ 1 - \left( \frac{\partial h}{\partial x} \right)^2 \right] + \tau_{zz} \frac{\partial h}{\partial x} - \tau_{xx} \frac{\partial h}{\partial x} \right\} = \frac{\partial \sigma}{\partial x} + \frac{\partial \sigma}{\partial z} \frac{\partial h}{\partial x}, \quad (2.5d)$$

$$-p + \frac{1}{1 + (\partial h / \partial x)^2} \left[ \tau_{zz} + \tau_{xx} \left( \frac{\partial h}{\partial x} \right)^2 - 2 \tau_{xz} \frac{\partial h}{\partial x} \right] = \sigma \frac{\partial^2 h / \partial x^2}{[1 + (\partial h / \partial x)^2]^{3/2}} \text{ at } z = h(x, t). \quad (2.5e)$$

In (2.5b,c),  $q$  denotes the rate of heat exchange between the free surface and the ambient air at temperature  $T_\infty$ . The kinematic boundary condition (2.5a) gives the interface location at time  $t$ , while the mass impermeability condition (2.5c) portrays the non-volatile behaviour of the binary mixture. The dynamics of the gas phase are decoupled here from the liquid phase by considering large differences in the physical properties between the two phases.

## 2.2. Constitutive model for the liquid

Viscoelastic liquids exhibit complex rheology under the simultaneous actions of viscous and elastic character. Unlike Newtonian liquids, stress exhibits here an elastic response to strain characterized by the relaxation time of the liquid. A wide variety of constitutive relationships, comprising both linear and nonlinear models, have been developed over the years to describe the rheology of viscoelastic liquids. In this analysis, we proceed with the linear Maxwell model (Maxwell 1867),

$$\boldsymbol{\tau} + \lambda \frac{\partial \boldsymbol{\tau}}{\partial t} = \mu_o [(\nabla \mathbf{v}) + (\nabla \mathbf{v})^T], \quad (2.6)$$

which characterizes the liquid by a single relaxation time  $\lambda$  (here  $\lambda$  is interpreted as the longest relaxation time out of the spectrum of relaxation times exhibited by a viscoelastic liquid) without incorporating the rheological nonlinearity. The reasons behind adopting this particular constitutive model for this investigation are as follows. First, in the present convection phenomenon, motion is developed in a liquid film which was at rest in its equilibrium state. This indicates that the shear rates involved with the underlying process are also extremely small. A nonlinear model (*viz.* the upper-convected Maxwell model, wherein the ordinary time derivative of  $\boldsymbol{\tau}$  in (2.6) is replaced by the ‘upper-convected’ time derivatives) is essential to describe the flow dynamics only at high shear rates. Second, since a linear stability analysis will be carried out around a quiescent base state, here any nonlinear terms in the constitutive equation will not make any contribution to the final linearized set of equations. Therefore, the stability picture obtained using a linear model will be identical to that with the inclusion of upper-convected terms. The aspects mentioned above suggest that the linearized Maxwell model is deemed sufficient to reveal the basic effect of elasticity for this analysis.

2.3. Non-dimensionalization

The boundary value problem (BVP) formulated by (2.3)–(2.5) is now non-dimensionalized by considering the unperturbed film thickness  $H$  as characteristic length scale, the thermal diffusion time  $H^2/\alpha$  as characteristic time scale and  $\vartheta H$  as temperature scale.

This allows us to define the following set of dimensionless variables:

$$\left. \begin{aligned} (\bar{x}, \bar{z}) &= \frac{(x, z)}{H}, \quad \bar{h} = \frac{h}{H}, \quad \bar{t} = \frac{t}{H^2/\alpha}, \quad (\bar{u}, \bar{w}) = \frac{u, w}{(\alpha/H)}, \quad \bar{\tau} = \frac{\tau}{\mu_o\alpha/H^2}, \\ \bar{p} &= \frac{p}{\mu_o\alpha/H^2}, \quad \bar{T} = \frac{T - T_\infty}{\vartheta H}, \quad \bar{c} = \frac{c}{\sigma_T\vartheta H/\sigma_c}. \end{aligned} \right\} \quad (2.7)$$

Note that, although the bulk concentration  $c$  (defined either as mass fraction or volume fraction) is a dimensionless quantity, its rescaling in the above-mentioned manner keeps this analysis coherent with the previously reported studies (Podolny *et al.* 2005; Shklyaev *et al.* 2009; Sarma & Mondal 2018). With this choice of the non-dimensional variables, we finally obtain the governing equations and the boundary conditions (dropping the overbar sign for notational convenience) in the following dimensionless form:

$$\nabla \cdot \mathbf{v} = 0, \tag{2.8a}$$

$$Pr^{-1} \left( \frac{\partial \mathbf{v}}{\partial t} + \mathbf{v} \cdot \nabla \mathbf{v} \right) = -\nabla p + \nabla \cdot \boldsymbol{\tau} - \mathbf{g}ak, \tag{2.8b}$$

$$\frac{\partial T}{\partial t} + \mathbf{v} \cdot \nabla T = \nabla^2 T, \tag{2.8c}$$

$$\frac{\partial c}{\partial t} + \mathbf{v} \cdot \nabla c = Le(\nabla^2 c + \chi \nabla^2 T); \tag{2.8d}$$

$$\mathbf{v} = 0, \quad \frac{\partial T}{\partial z} = -1, \quad \frac{\partial c}{\partial z} = \chi \quad \text{at } z = 0, \tag{2.9a-c}$$

$$w = \frac{\partial h}{\partial t} + u \frac{\partial h}{\partial x}, \tag{2.10a}$$

$$\left( \frac{\partial T}{\partial z} - \frac{\partial h}{\partial x} \frac{\partial T}{\partial x} \right) + BiT \sqrt{1 + (\partial h/\partial x)^2} = 0, \tag{2.10b}$$

$$\left( \frac{\partial c}{\partial z} - \frac{\partial h}{\partial x} \frac{\partial c}{\partial x} \right) - \chi BiT \sqrt{1 + (\partial h/\partial x)^2} = 0, \tag{2.10c}$$

$$-p + \frac{1}{1 + (\partial h/\partial x)^2} \left[ \tau_{zz} + \tau_{xx} \left( \frac{\partial h}{\partial x} \right)^2 - 2\tau_{xz} \frac{\partial h}{\partial x} \right] = \Sigma \frac{\partial^2 h/\partial x^2}{[1 + (\partial h/\partial x)^2]^{3/2}}, \tag{2.10d}$$

$$\begin{aligned} & \frac{1}{\sqrt{1 + (\partial h/\partial x)^2}} \left\{ \tau_{xz} \left[ 1 - \left( \frac{\partial h}{\partial x} \right)^2 \right] + \tau_{zz} \frac{\partial h}{\partial x} - \tau_{xx} \frac{\partial h}{\partial x} \right\} \\ & = Ma \left[ -\frac{\partial T}{\partial x} + \frac{\partial c}{\partial x} + \left( -\frac{\partial T}{\partial z} + \frac{\partial c}{\partial z} \right) \frac{\partial h}{\partial x} \right] \text{ at } z = h(x, t). \end{aligned} \tag{2.10e}$$

Moreover, in non-dimensional form, the Maxwell constitutive model (2.6) reads

$$\boldsymbol{\tau} + De \frac{\partial \boldsymbol{\tau}}{\partial t} = [(\nabla \mathbf{v}) + (\nabla \mathbf{v})^T]. \tag{2.11}$$

This problem is now characterized by the following set of dimensionless parameters: the Marangoni number  $Ma$ , the Prandtl number  $Pr$ , the Deborah number  $De$ , the (inverse) Lewis number  $Le$ , the Soret number  $\chi$ , the Biot number  $Bi$ , the Galileo number  $Ga$ , and the (inverse) capillary number  $\Sigma$ :

$$\left. \begin{aligned} Ma &= \frac{\sigma_T \vartheta H^2}{\mu_o \alpha}, & Pr &= \frac{\mu_o}{\rho \alpha}, & De &= \frac{\lambda \alpha}{H^2}, & Le &= \frac{D}{\alpha}, \\ \chi &= \frac{S \sigma_c}{\sigma_T}, & Bi &= \frac{qH}{\kappa}, & Ga &= \frac{\rho g H^3}{\mu_o \alpha}, & \Sigma &= \frac{\sigma H}{\mu_o \alpha} \end{aligned} \right\} \quad (2.12)$$

The Marangoni number governs the present instability phenomenon. For the convection to set in, the thermosolutocapillary stresses must have to overcome the stabilization effects of viscous and thermal diffusion. The Marangoni number  $Ma$  gives the critical temperature difference across the film ( $\vartheta H$ ) at which convection appears in the film. Note that, for  $\sigma_T > 0$ ,  $Ma$  can assume both positive and negative values depending on the direction of the applied temperature gradient  $\vartheta$ . A positive (negative)  $Ma$  indicates that the liquid layer is subjected to heating from below (above). However, we restrict this analysis only to positive values of  $Ma$ . The Prandtl number  $Pr$  is a material property of the liquid. Excluding the rarefied gases (which display a strong viscoelastic character with  $Pr \ll 1$ ), for most viscoelastic liquids  $Pr \gg 1$ . This indicates a larger thermal diffusion time scale ( $H^2/\alpha$ ) compared to the viscous diffusion time scale ( $\rho H^2/\mu_o$ ) for such liquids. The Deborah number  $De$  is a measure of elasticity of the liquid. The value  $De = 0$  indicates a Newtonian liquid ( $\lambda = 0$ ), while higher values of  $De$  signify enhanced elastic behaviour of the liquid. The (inverse) Lewis number  $Le$  compares the characteristic mass diffusion time scale  $H^2/D$  to the thermal diffusion time scale  $H^2/\alpha$ . Usually  $Le$  is small for binary liquid mixtures and lies within  $10^{-5} \leq Le \leq 10^{-1}$ . The Soret number  $\chi$  takes into account the relative contributions of thermocapillary and solutocapillary forces to the free surface force. Note that  $\chi$  can be either positive or negative based on the Soret coefficient  $S$  (see § 2.2). The typical value of  $\chi$  varies within  $-1 \leq \chi \leq 1$ . The Biot number  $Bi$  characterizes the heat transfer rate across the free surface. The Galileo number  $Ga$  and the (inverse) capillary number  $\Sigma$  take account of the free surface deformability through the magnitude of  $g$  and  $\sigma$ . For a 0.1 mm thick layer of a polymeric solution with  $\mu_o = O(10^{-2})$  Pa s,  $\rho = O(10^3)$  kg m $^{-3}$ ,  $\alpha = O(10^{-7})$  m $^2$  s $^{-1}$ ,  $\sigma = O(10^{-2})$  N m $^{-1}$  and  $g = O(0.1)$  m s $^{-2}$ , we obtain  $Ga = 0.1$ , which corresponds to the microgravity environment. It is important to note that a free surface can be treated as non-deformable in the limit  $(Ga, \Sigma) \rightarrow \infty$ , which is usually the case for a liquid layer with very high surface tension in the terrestrial environment. In order to reveal the role of surface deformability on the stability characteristics of the system, we consider here two separate cases: (i)  $(Ga, \Sigma) = (0.1, 10^3)$ , which represents a liquid layer with a deformable free surface in the microgravity environment, and (ii)  $(Ga, \Sigma) \rightarrow \infty$ , which refers to a liquid layer with a non-deformable free surface.

### 3. Basic state and linear stability analysis

In this section, we present a linear stability analysis for small perturbations around the quiescent liquid film with laterally uniform temperature and concentration distribution.



This purely conductive state of the system is represented by

$$\left. \begin{aligned} \mathbf{v}^o &= 0, & \boldsymbol{\tau}^o &= 0, & h^o &= 1, & p^o &= Ga(1 - z), \\ T^o &= 1 - z + Bi^{-1}, & c^o &= \chi z + \text{const.}, \end{aligned} \right\} \quad (3.1a-f)$$

which are steady-state solutions of (2.8)–(2.10). One can notice that the elasticity of the liquid does not influence this basic state. We now study the stability of this basic state by introducing the following two-dimensional infinitesimal normal perturbations (denoted by a tilde) to the steady-state solutions (3.1):

$$\left. \begin{aligned} \mathbf{v} &= \mathbf{v}^o + \tilde{\mathbf{v}}(x, z, t), & \boldsymbol{\tau} &= \boldsymbol{\tau}^o + \tilde{\boldsymbol{\tau}}(x, z, t), & p &= p^o + \tilde{p}(x, z, t), \\ T &= T^o + \tilde{\theta}(x, z, t), & h &= h^o + \tilde{\xi}(x, z, t), & c &= c^o + \tilde{c}(x, z, t). \end{aligned} \right\} \quad (3.2a-f)$$

Linearization of (2.8)–(2.10) by neglecting the terms nonlinear in perturbations yields the following set of governing equations and boundary conditions:

$$\nabla \cdot \tilde{\mathbf{v}} = 0, \quad (3.3a)$$

$$Pr^{-1} \frac{\partial \tilde{\mathbf{v}}}{\partial t} = -\nabla \tilde{p} + \nabla \cdot \tilde{\boldsymbol{\tau}}, \quad (3.3b)$$

$$\frac{\partial \tilde{\theta}}{\partial t} = \nabla^2 \tilde{\theta} + \tilde{w}, \quad (3.3c)$$

$$\frac{\partial \tilde{c}}{\partial t} + \chi \tilde{w} = Le(\nabla^2 \tilde{c} + \chi \nabla^2 \tilde{T}); \quad (3.3d)$$

$$\tilde{\mathbf{v}} = 0, \quad \frac{\partial \tilde{\theta}}{\partial z} = 0, \quad \frac{\partial \tilde{c}}{\partial z} = 0 \quad \text{at } z = 0, \quad (3.4a-c)$$

$$\left. \begin{aligned} \frac{\partial \tilde{\xi}}{\partial t} &= \tilde{w}, & \frac{\partial \tilde{\theta}}{\partial z} &= -Bi(\tilde{\theta} - \tilde{\xi}), & \frac{\partial \tilde{c}}{\partial z} &= \chi Bi(\tilde{\theta} - \tilde{\xi}), \\ \tilde{\tau}_{xz} &= Ma \frac{\partial}{\partial x} (\tilde{c} - \tilde{\theta} + \tilde{\xi} + \chi \tilde{\xi}), & -\tilde{p} + Ga \tilde{\xi} + \tilde{\tau}_{zz} &= \Sigma \frac{\partial^2 \tilde{\xi}}{\partial x^2} \quad \text{at } z = 1, \end{aligned} \right\} \quad (3.5a-e)$$

whereas the constitutive equation (2.11) reads

$$\tilde{\boldsymbol{\tau}} + De \frac{\partial \tilde{\boldsymbol{\tau}}}{\partial t} = [(\nabla \tilde{\mathbf{v}}) + (\nabla \tilde{\mathbf{v}})^T]. \quad (3.6)$$

We now cast the BVP (3.3)–(3.5) in terms of the streamfunction  $\tilde{\psi}(x, z, t)$  so that

$$\tilde{u} = \frac{\partial \tilde{\psi}}{\partial z}, \quad \tilde{w} = -\frac{\partial \tilde{\psi}}{\partial x}. \quad (3.7a,b)$$

The basic idea behind the streamfunction formulation is to eliminate the pressure term  $\tilde{p}$  from the system of equations (3.3)–(3.5). Introducing relationships (3.7) and the constitutive equation for Maxwell viscoelastic model (3.6) into (3.3)–(3.5), we finally

arrive at

$$Pr^{-1} \left( \frac{\partial}{\partial t} \nabla^2 \tilde{\psi} + De \frac{\partial^2}{\partial t^2} \nabla^2 \tilde{\psi} \right) = \nabla^4 \tilde{\psi}, \tag{3.8a}$$

$$\frac{\partial \tilde{\theta}}{\partial t} = \nabla^2 \tilde{\theta} - \frac{\partial \tilde{\psi}}{\partial x}, \tag{3.8b}$$

$$\frac{\partial \tilde{c}}{\partial t} - \chi \frac{\partial \tilde{\psi}}{\partial x} = Le[\nabla^2 \tilde{c} + \chi \nabla^2 \tilde{T}], \tag{3.8c}$$

with the boundary conditions

$$\tilde{\psi} = 0, \quad \frac{\partial \tilde{\psi}}{\partial z} = 0, \quad \frac{\partial \tilde{\theta}}{\partial z} = 0, \quad \frac{\partial \tilde{c}}{\partial z} = 0 \quad \text{at } z = 0, \tag{3.9a-d}$$

$$\frac{\partial \tilde{\xi}}{\partial t} = -\frac{\partial \tilde{\psi}}{\partial x}, \quad \frac{\partial \tilde{\theta}}{\partial z} = -Bi(\tilde{\theta} - \tilde{\xi}), \quad \frac{\partial \tilde{c}}{\partial z} = \chi Bi(\tilde{\theta} - \tilde{\xi}), \tag{3.10a-c}$$

$$\frac{\partial^2 \tilde{\psi}}{\partial z^2} - \frac{\partial^2 \tilde{\psi}}{\partial x^2} = Ma \frac{\partial}{\partial x} (\tilde{c} - \tilde{\theta} + \tilde{\xi} + \chi \tilde{\xi}) + Ma De \frac{\partial^2}{\partial t \partial x} (\tilde{c} - \tilde{\theta} + \tilde{\xi} + \chi \tilde{\xi}), \tag{3.10d}$$

$$\left( 1 + De \frac{\partial}{\partial t} \right) \left( \Sigma \frac{\partial^3 \tilde{\xi}}{\partial x^3} - Pr^{-1} \frac{\partial^2 \tilde{\psi}}{\partial t \partial z} - Ga \frac{\partial \tilde{\xi}}{\partial x} \right) = -\frac{\partial}{\partial z} \left( 3 \frac{\partial^2}{\partial x^2} + \frac{\partial^2}{\partial z^2} \right) \tilde{\psi} \quad \text{at } z = 1. \tag{3.10e}$$

Noticing that the basic state (3.1) is invariant with respect to  $x$  and  $t$ , we use the Fourier decomposition to separate the  $x$  and  $t$  dependences of the perturbed fields ( $\tilde{\psi}$ ,  $\tilde{\theta}$ ,  $\tilde{c}$ ,  $\tilde{\xi}$ ) from that with  $z$ :

$$(\tilde{\psi}(x, z, t), \tilde{\theta}(x, z, t), \tilde{c}(x, z, t), \tilde{\xi}(x, z, t)) = (\hat{\psi}(z), \hat{\theta}(z), \hat{c}(z), \hat{\xi}(z)) \exp(ikx - \lambda t), \tag{3.11}$$

where ( $\hat{\psi}$ ,  $\hat{\theta}$ ,  $\hat{c}$ ,  $\hat{\xi}$ ) are the amplitudes of perturbations,  $k$  denotes the dimensionless horizontal wavenumber and  $\lambda = \Omega + i\omega$  refers to the decay rate of perturbations. The parameter  $\omega$  (a real quantity) represents the frequency of perturbation. Hence, the dynamics of these infinitesimal perturbations is now governed by the following eigenvalue problem (EVP):

$$Pr \frac{d^4 \hat{\psi}}{dz^4} - (\lambda^2 De - \lambda + 2Prk^2) \frac{d^2 \hat{\psi}}{dz^2} + (\lambda^2 De - \lambda + Prk^2) k^2 \hat{\psi} = 0, \tag{3.12a}$$

$$\frac{d^2 \hat{\theta}}{dz^2} + (\lambda - k^2) \hat{\theta} = ik \hat{\psi}, \tag{3.12b}$$

$$Le \frac{d^2 \hat{c}}{dz^2} + (\lambda - Lek^2) \hat{c} = -Le\chi \left( \frac{d^2 \hat{\theta}}{dz^2} - k^2 \hat{\theta} \right) - i\chi k \hat{\psi}; \tag{3.12c}$$

$$\hat{\psi} = 0, \quad \frac{d\hat{\psi}}{dz} = 0, \quad \frac{d\hat{\theta}}{dz} = 0, \quad \frac{d\hat{c}}{dz} = 0 \quad \text{at } z = 0, \tag{3.13a-d}$$

$$ik \hat{\psi} = \lambda \hat{\xi}, \quad \frac{d\hat{\theta}}{dz} = -Bi(\hat{\theta} - \hat{\xi}), \quad \frac{d\hat{c}}{dz} = \chi Bi(\hat{\theta} - \hat{\xi}), \tag{3.14a-c}$$

$$\frac{d^2 \widehat{\psi}}{dz^2} + k^2 \widehat{\psi} = iMa k(1 - \lambda De)(\widehat{c} - \widehat{\theta} + \chi \widehat{\xi} + \widehat{\xi}), \quad (3.14d)$$

$$Pr \frac{d^3 \widehat{\psi}}{dz^3} + (\lambda - \lambda^2 De - 3Prk^2) \frac{d\widehat{\psi}}{dz} = ikPr(1 - \lambda De)(Ga + \Sigma k^2) \widehat{\xi} \quad \text{at } z = 1, \quad (3.14e)$$

with  $\lambda$  and  $Ma$  as the eigenvalues. This problem was recently analysed by Sarma & Mondal (2019) for a *pure* viscoelastic film ( $Le, \chi \rightarrow 0$ ). Surpassing this restriction, the more realistic binary aspect of the liquid is considered here, along with the incorporation of the Soret effect. Solving the system (3.12)–(3.14) for  $\Omega = 0$ , one can now obtain the neutral stability curves that demarcate the stable regime from the unstable one. However, the complexity of solvability conditions here restrains us from taking an analytical approach. Therefore, the EVP is solved numerically using the fourth-order Runge–Kutta method with shooting technique (Keller 2018) for disturbances with arbitrary values of  $k$ . An approximate model will be developed in § 6 in the asymptotic limit  $k \rightarrow 0$ .

It is well known that, provided with a good initial guess, the shooting method usually yields a more accurate solution at reduced computational cost compared to most other numerical methods (McFadden, Coriell & Lott 2010; Hirata *et al.* 2015). We have verified the accuracy of our numerical scheme by comparing the results with those available in the literature as well as with the results obtained from the approximate model. However, confronted by the lack of published results on the thermosolutal Marangoni convection for viscoelastic liquids, we first test the accuracy of our numerical solution against the results of Shklyayev *et al.* (2009). These authors numerically investigated the instability problem for a Newtonian binary mixture. In figure 2, one can see that an excellent quantitative agreement exists between the present results and the computations of Shklyayev *et al.* (2009) for both values of  $Bi$ . The numerical results are also found to agree well with the results of the approximate model (see figures 14–16) for all but the parameter values that violate the approximations necessary to derive the model (discussed in § 6). These comparisons ensure the accuracy of the present numerical scheme for the entire parametric range of interest.

The EVP posed by (3.12)–(3.14) suggests the possible emergence of two different instability modes in the system: (i) monotonic mode (or stationary convection) and (ii) oscillatory mode (or overstability) for which the disturbances grow with temporal oscillations. The stability thresholds for the monotonic and oscillatory modes can be obtained from (3.12)–(3.14) by substituting  $\lambda = 0$  and  $\lambda = i\omega$ , respectively. Note that, to find the stability margin for the oscillatory instability mode, we numerically seek such a value of  $\omega$  for which the imaginary part of  $Ma$  vanishes. Repetition of this procedure for a broad range of  $k$  yields the neutral stability curve for this particular instability mode.

#### 4. The linear stability picture

In this section, we analyse the stability picture obtained through numerical computations. Emphasis is put on understanding how viscoelasticity in the presence of the Soret effect deviates the stability characteristics of the system from its Newtonian counterpart. For convenience in analysis, we divide the entire disturbance spectrum into two different regimes: (i) long-wave regime,  $k < O(1)$ , and (ii) short-wave regime,  $k \gtrsim O(1)$ . Furthermore, it is important to remark that we fix  $Pr = 10$  for all the graphical results. This is because the stability margin shows no substantial variation with  $Pr$

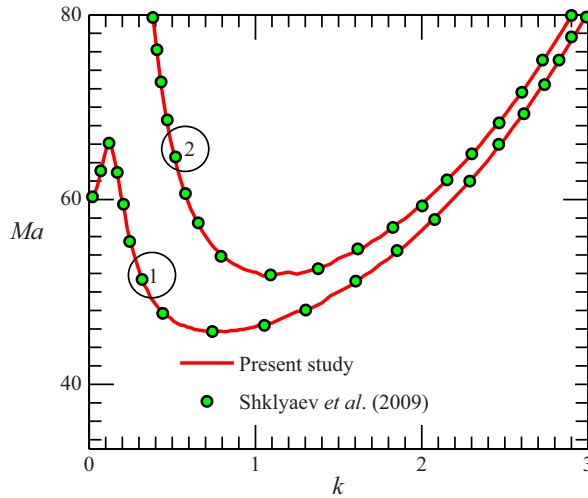


FIGURE 2. Comparison of the present numerical result with the results of Shklyaev *et al.* (2009) (shown by markers ‘o’) via the neutral stability curve at  $Pr = 2$ ,  $\chi = -0.2$  and  $Le = 10^{-3}$ . Curves marked by 1 and 2 correspond to  $Bi = 0$  and  $Bi = 0.1$  respectively. To represent the characteristics of a Newtonian binary liquid with a non-deformable free surface, we consider  $De = 0$  and  $(Ga, \Sigma) \rightarrow \infty$ .

against both the long-wave and short-wave perturbations (this is also apparent from the approximate model derived in § 6).

#### 4.1. Effect of elasticity and the free surface deformability

Let us first start with the monotonic instability mode. Figure 3 plots the neutral stability curves for this particular instability mode. The solid line here represents the stability threshold for a liquid layer with a deformable free surface  $(Ga, \Sigma) = (0.1, 10^3)$ , while the dotted one depicts the stability margin for a non-deformable surface  $(Ga, \Sigma) \rightarrow \infty$ . It can be observed that, over the entire range of disturbance wavenumber  $k$ , there exists a minimum value for the Marangoni number  $Ma$  (indicated by the marker ‘o’; see inset of figure 3) only above which the instability first sets in in the system. We call this  $Ma$  the critical Marangoni number ( $Ma_c$ ) and the corresponding  $k$  and  $\omega$  as the critical wavenumber ( $k_c$ ) and critical oscillation frequency ( $\omega_c$ ), respectively.

From figure 3 it is clear that, irrespective of the free surface deformability, the monotonic disturbances always emerge in the long-wave form ( $k_c \ll O(1)$ ). Nevertheless, the increased gravitational and surface tension forces for a non-deformable surface slightly delay the onset of these disturbances in the system ( $Ma_{c,(Ga,\Sigma)\rightarrow\infty} > Ma_{c,(Ga,\Sigma)\rightarrow(0.1,10^3)}$ ; see inset of figure 3). Notably, the monotonic instability threshold is not affected by the elastic behaviour of the liquid. This is due to the vanishing of any temporal components for this stationary convection (cf. (3.12)–(3.14) substituting  $\lambda = 0$ ). The role of other non-dimensional parameters on the stability margin for this instability mode will be discussed systematically in the subsequent subsections.

We now focus our attention on the disturbances that emerge with temporal oscillations ( $\omega \neq 0$ ), giving rise to Hopf bifurcation. Previous investigations on the pure thermocapillary instability in a viscoelastic film (Lebon *et al.* 1994; Parmentier *et al.* 2000; Ramkissoon *et al.* 2006) suggest that the oscillatory disturbances are more

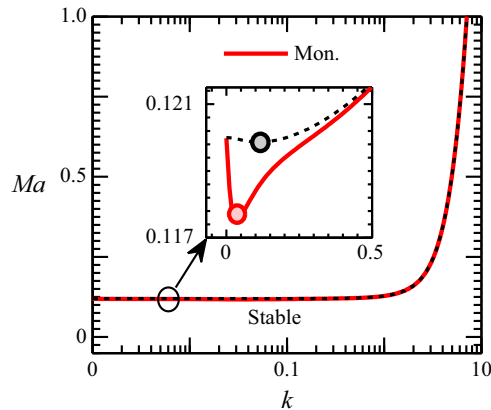


FIGURE 3. Neutral stability curves  $Ma(k)$  for the monotonic instability mode. The solid line represents the stability threshold for a deformable free surface  $(Ga, \Sigma) = (0.1, 10^3)$ , whereas the dotted line demonstrates the stability margin for a non-deformable free surface  $(Ga, \Sigma) \rightarrow \infty$ . The dot (o) mark on each neutral curve represents the critical point of the curve. The inset depicts the effect of free surface deformability on the stability threshold in the long-wave regime. Other parameters:  $Bi = 0.01$ ,  $\chi = 0.5$ ,  $Le = 10^{-3}$  and  $Pr = 10$ .

likely to appear in a highly viscoelastic film (highly and weakly viscoelastic liquids will be defined shortly). For the present thermosolutal convection process, we will demonstrate that, depending on the nature of the Soret coefficient (i.e. whether  $\chi > 0$  or  $\chi < 0$ ), two different oscillatory instabilities can emerge in the system. We call them the oscillatory-I and oscillatory-II modes. It is important to remark that the characteristics of the oscillatory-I mode have been extensively studied in the literature in the context of a Newtonian binary mixture (Skarda *et al.* 1998; Podolny *et al.* 2005; Shklyaev *et al.* 2009; Bestehorn & Borcia 2010). However, its behaviour for a viscoelastic binary liquid has not been investigated yet. On the other hand, to our knowledge, the oscillatory-II mode has remained entirely unexplored, even for a Newtonian binary liquid (perhaps due to limited examination over the model parameters). We will demonstrate that, for a viscoelastic binary mixture, while the oscillatory-I mode is more universal, the oscillatory-II instability can also become dominant in the system under appropriate model parameter values.

Figure 4 plots the neutral stability curves as well as the corresponding oscillation frequencies for the oscillatory-I mode. The solid and the dash-dotted lines represent here the stability margin for a deformable free surface, while their adjacent dotted lines depict the stability boundary for a non-deformable free surface.

Figure 4(a) demonstrates that, for  $\chi < 0$ , the neutral curves consist of two branches, each characterized by a distinct local minimum. Note that, of these two minima, while one resides in the long-wave regime ( $k_c < O(1)$ ), the other lies in the short-wave regime ( $k_c \approx O(1)$ ). Accordingly, we call these branches the long-wave and short-wave branch, respectively. It can be clearly seen that, for the long-wave branch,  $Ma_c$  is a strong function of the deformability of the free surface. Similar to the monotonic mode, a reduced free surface deformability enhances the stability of the system against the long-wave oscillatory-I disturbances as well. However, the onset of these disturbances essentially remains unaffected by the elastic behaviour of the liquid (see figure 4a; the long-wave branch for  $De = 0$  and 1 merge into a single curve). On the other hand,  $Ma_c$  for the short-wave branch is not influenced by the deformability of the free surface, but is

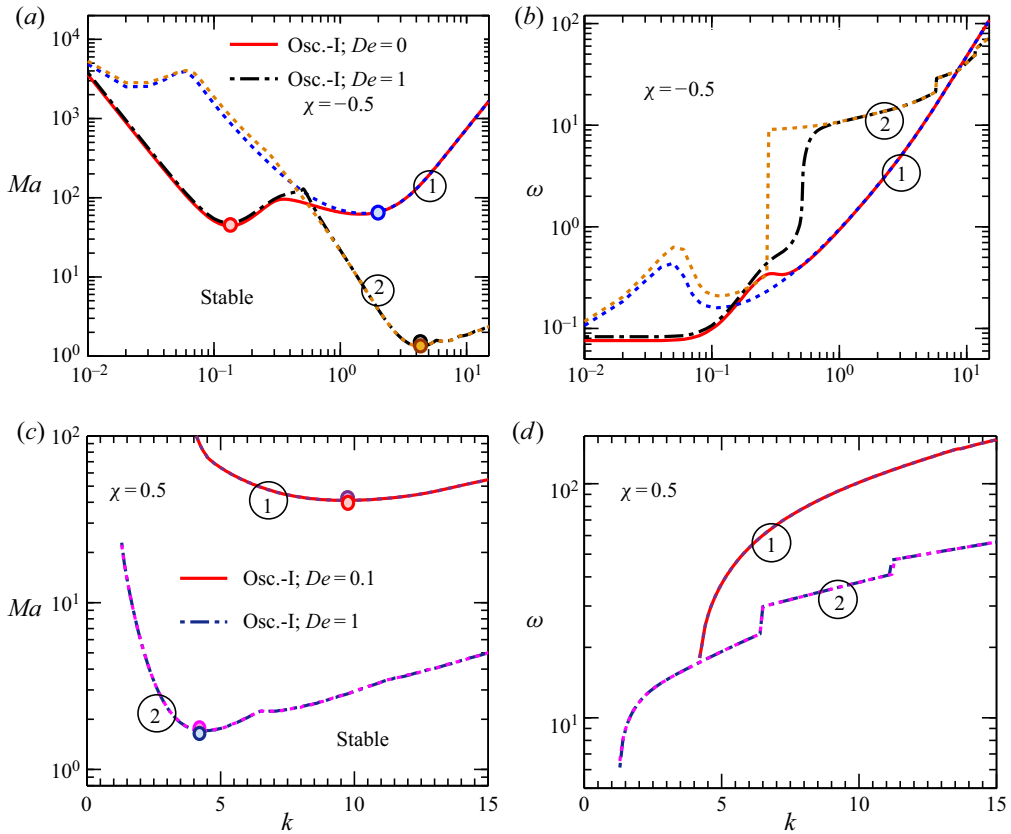


FIGURE 4. (a,c) Neutral stability curves  $Ma(k)$ , and (b,d) the corresponding oscillation frequency  $\omega$  for the oscillatory-I instability mode for  $\chi < 0$  ( $= -0.5$ ) and  $\chi > 0$  ( $= 0.5$ ), respectively. For panels (a,b), the lines marked by 1 and 2 correspond to  $De = 0$  and  $De = 1$ , respectively; for panels (c,d), the lines marked by 1 and 2 correspond to  $De = 0.1$  and  $De = 1$ , respectively. In each panel, the solid and the dash-dotted lines depict the results for a deformable free surface  $(Ga, \Sigma) = (0.1, 10^3)$ ; the adjacent dotted line represents the results for a non-deformable free surface  $(Ga, \Sigma) \rightarrow \infty$ . The dot (o) mark on each neutral curve denotes the critical point (or the global minimum) of the curve. Other parameters:  $Bi = 0.1$ ,  $Le = 0.01$  and  $Pr = 10$ .

governed by the elasticity of the mixture. An increased elasticity of the liquid substantially promotes here the onset of instability in the system. This suggests that, depending on the free surface deformability and the elasticity level of the liquid, either of the long-wave or short-wave branches can hold the position of global minimum (see the marker ‘o’ on each neutral curve in figure 4a). In other words, the oscillatory-I disturbances can emerge in both the long-wave and short-wave form for  $\chi < 0$ .

Figure 4(c) shows that, for  $\chi > 0$ , the long-wave branch disappears, leaving only the short-wave branch. In particular, in this regime of  $\chi$ , the oscillatory-I disturbances are found only for  $De > 0$ . This indicates that the emergence of short-wave oscillatory-I instability for  $\chi > 0$  is a sole manifestation of the elastic behaviour of the liquid. Similarly to the case  $\chi < 0$ , the stability threshold remains unaltered by the deformability of the free surface but diminishes drastically with the increasing elasticity of the mixture.

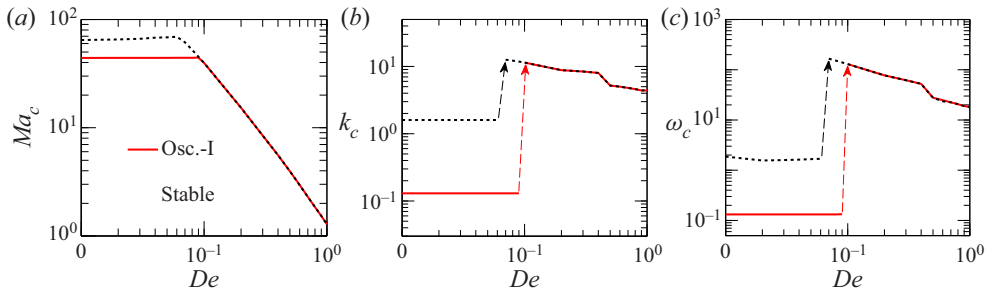


FIGURE 5. Variation of the (a) critical Marangoni number  $Ma_c$ , and the corresponding critical (b) wavenumber  $k_c$  and (c) oscillation frequency  $\omega_c$  with Deborah number  $De$  for the oscillatory-I instability mode for  $\chi < 0$ . The solid line depicts the variation for a deformable free surface  $(Ga, \Sigma) = (0.1, 10^3)$ ; and the dotted line is that for a non-deformable surface  $(Ga, \Sigma) \rightarrow \infty$ . The arrow marks in panels (b,c) illustrate a switchover in the instability behaviour with the increasing elasticity of the liquid. Other parameters:  $Bi = 0.1$ ,  $Le = 0.01$  and  $\chi = -0.5$ .

The oscillation frequency  $\omega$  of the neutral perturbations corresponding to each neutral curve of figure 4(a,c) is plotted in figure 4(b,d). The deformability of the free surface controls  $\omega$  only in the long-wave regime, whereas  $\omega$  is primarily modulated by the elasticity of the liquid in the short-wave regime. It should be further noted that, although the  $\omega(k)$  variation is smooth in the long-wave regime, discontinuity appears in the short-wave regime (in particular at higher values of  $De$ ). In the neighbourhood of such points of discontinuity, a sudden change in the gradient of  $Ma(k)$  neutral curve occurs, as can be observed from figure 4(a,c). Similar features of the neutral curves have been reported previously by Dauby *et al.* (1993) and Parmentier *et al.* (2000) in the context of pure thermocapillary-driven convection in a viscoelastic film.

It is now clear that, for  $\chi < 0$ , the oscillatory-I disturbances can develop in both Newtonian and viscoelastic binary mixtures. However, the elasticity of the liquid significantly influences the onset of this particular instability mode in the system. To illustrate this elasticity-based transition of the stability picture, we plot in figure 5 the critical Marangoni number  $Ma_c$ , the corresponding wavenumber  $k_c$ , and oscillation frequency  $\omega_c$  as functions of Deborah number  $De$  for both the cases of deformable (solid line) and non-deformable (dotted line) free surface. Note that  $Ma_c$  refers here to the global minimum of the oscillatory-I neutral curve. Two regimes are clearly distinguishable from the variations depicted by figure 5: a weakly elastic regime (for  $De \lesssim 0.1$ ) wherein the stability behaviour resembles that of a Newtonian binary liquid (at least for bifurcation around the conductive base state), and a strong elastic regime (for  $De > 0.1$ ) where the elasticity of the liquid governs the stability threshold and the critical parameters ( $k_c$ ,  $\omega_c$ ). The transition between these two regimes is marked by sharp discontinuities in  $k_c$  and  $\omega_c$  (see the arrow marks in figure 5b,c).

A key observation from figure 5 is that, in the weakly elastic regime, while the critical parameters ( $Ma_c$ ,  $k_c$ ,  $\omega_c$ ) are governed by the deformability of the free surface rather than the elasticity of the liquid, the opposite is true for the highly elastic regime. Figure 5(a) shows that the reducing deformability of the free surface dampens the onset of oscillatory-I instability for  $De \lesssim 0.1$ . The resulting disturbances emerge in the long-wave form ( $k_c \approx 0.1$ ) for a deformable free surface and the short-wave form ( $k_c \approx 1$ ) in case of a non-deformable free surface (see figure 5b). On the other hand, for a highly viscoelastic

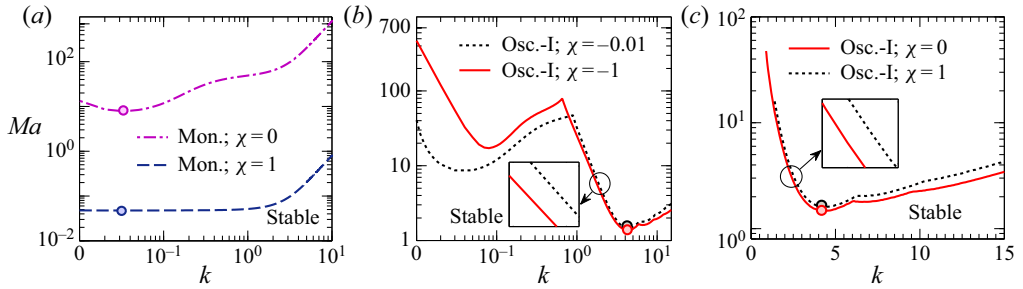


FIGURE 6. Neutral stability curves  $Ma(k)$  for the monotonic and oscillatory-I modes in the (a,c) positive and (b) negative Soret number  $\chi$  domains. The long-wave branch for the oscillatory-I mode emerges only when  $\chi < 0$ . The dot (o) mark on each neutral curve represents the critical point of the curve. Other parameters:  $Bi = 0.01$ ,  $De = 1$ ,  $Le = 10^{-3}$  and  $(Ga, \Sigma) = (0.1, 10^3)$ .

mixture ( $De > 0.1$ ), irrespective of the free surface deformability, the disturbances always set in in the short-wavelength form. An inverse variation of the parameters ( $Ma_c, k_c, \omega_c$ ) with  $De$  in this regime suggests that, for the enhanced elasticity of the binary mixture, the conductive state is more likely to bifurcate to the short-wave oscillatory-I mode with a more easily detectable convective pattern.

Another interesting feature presented by figure 5 is that, for  $De \approx 0.1$  (i.e. the boundary separating the weakly and highly elastic regimes for a liquid layer with a deformable free surface),  $Ma_c$  for the onset of long-wave and short-wave oscillatory-I perturbations coincide. Therefore, a competition between the respective instability modes can take place in the system for  $(De, Ga, \Sigma) \approx (0.1, 0.1, 10^3)$ .

#### 4.2. The role of thermocapillary and solutocapillary effects

In this subsection, we investigate the contributions of thermocapillary and solutocapillary forces on the development of instabilities in the system. This is done by plotting the neutral stability curves for monotonic and oscillatory modes at different values of  $\chi$ . Recall that  $\chi = 0$  refers in this analysis to the case of purely thermocapillary-driven convection. Figure 6(a) shows that the domain of stability reduces substantially as  $\chi$  increases from zero. This suggests that both thermocapillary and solutocapillary forces play a destabilizing role in the emergence of monotonic instability for  $\chi > 0$ . However, it is important to note that  $k_c$  for this instability mode is not decided by the solutal effects (at least for a deformable surface; the case of a non-deformable surface will be discussed in figure 7). Although not shown here graphically, this particular instability mode can appear even for  $\chi < 0$ , within a narrow interval of  $\chi$ . This range will be identified in § 6, performing a long-wave asymptotic analysis of the problem.

Figure 6(b) demonstrates that, for the long-wave branch of oscillatory-I mode, solutocapillarity acts as stabilizing, while thermocapillarity turns into the destabilizing mechanism. Such opposite contributions of the driving forces give rise to the long-wave oscillatory-I perturbations in the system. On the other hand, thermocapillarity, coupled with the elasticity of the liquid, primarily give rise to the short-wave disturbances. Solutocapillarity provides here only a small correction to the stability margin. Interestingly, for this short-wave branch, an increasing  $|\chi|$  in the range  $\chi < 0$  weakly destabilizes the system, whereas an increment in  $\chi$  for  $\chi > 0$  leads to a mild stabilization of the system (see insets in figure 6b,c).



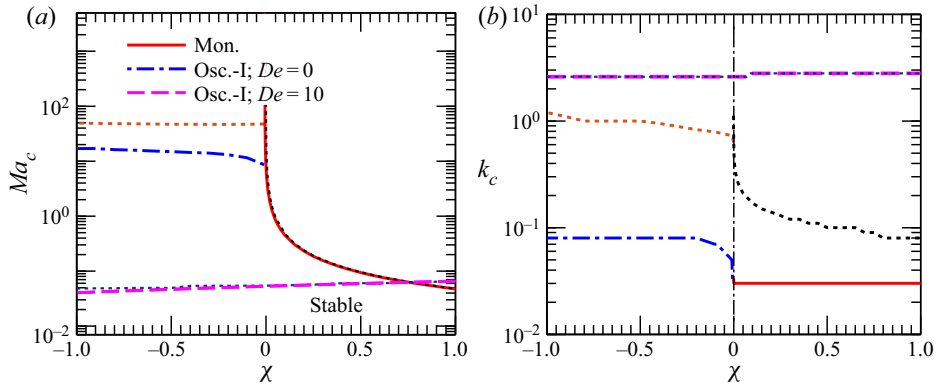


FIGURE 7. Variation of the (a) critical Marangoni number  $Ma_c$ , and the corresponding (b) critical wavenumber  $k_c$  with  $\chi$ . In each panel, the solid, dash-dotted and dashed lines represent the variations for a deformable free surface  $(Ga, \Sigma) = (0.1, 10^3)$ . The dotted lines adjacent to each instability mode represent the variations for a non-deformable free surface  $(Ga, \Sigma) \rightarrow \infty$ . Other parameters:  $Bi = 0.01$  and  $Le = 10^{-3}$ .

Figure 7 plots the variations of critical Marangoni number  $Ma_c$  and the corresponding wavenumber  $k_c$  with  $\chi$  for the cases of both a deformable and a non-deformable free surface. Clearly, an increasing  $\chi$  ( $> 0$ ) leads to a strong destabilization of the system with respect to the monotonic disturbances (see figure 7a). It should be noted that, for this instability mode, although the deformability of the free surface only weakly influences the stability threshold (see figure 3; this is not even perceptible in the scale of figure 7a), nevertheless, it plays an important role in determining the size of the convection cells. In figure 7(b) one can see that  $k_{c,(Ga,\Sigma)\rightarrow\infty} > k_{c,(Ga,\Sigma)=(0.1,10^3)}$ , implying that a highly deformable free surface allows the formation of much larger sized stationary convective patterns compared to its non-deformable counterpart.

For the oscillatory-I mode, figure 7(a) shows that an increasing  $|\chi|$  augments the stability region for a Newtonian binary liquid film having a deformable free surface. However, in the case of a non-deformable free surface (or for a highly viscoelastic mixture irrespective of the free surface deformability), the stability thresholds are found to remain nearly independent of  $\chi$ . In this regard, it is important to observe in figure 7(b) that, for a Newtonian binary mixture with a deformable surface,  $k_c$  lies in the long-wave regime, whereas, for a non-deformable surface (or for a highly viscoelastic mixture),  $k_c$  resides in the short-wave regime. The fact that the solutocapillary effect is dominant only in the long-wave regime (see figure 6) thus explains the variations in figure 7(a).

Before concluding this subsection, an additional remark about figure 7(a) is necessary. Note that, at the intersection point between the neutral curves for monotonic and oscillatory-I modes,  $Ma_{c,mon} = Ma_{c,osc-I}$ . Therefore, a competition between the respective instability modes can occur for  $\chi$  values corresponding to this point. Now, for  $De > 0$ , since the oscillatory-I disturbances can appear for any  $\chi \in \mathbb{R}$ , and as their onset gets triggered by the increasing elasticity of the liquid, the neutral curve for the monotonic mode presented in figure 7(a) is essentially the locus of codimension-two bifurcation points. Towards the left of this curve, the conductive state bifurcates into the oscillatory-I mode, while a steady bifurcation (i.e. monotonic instability) takes place on its right.

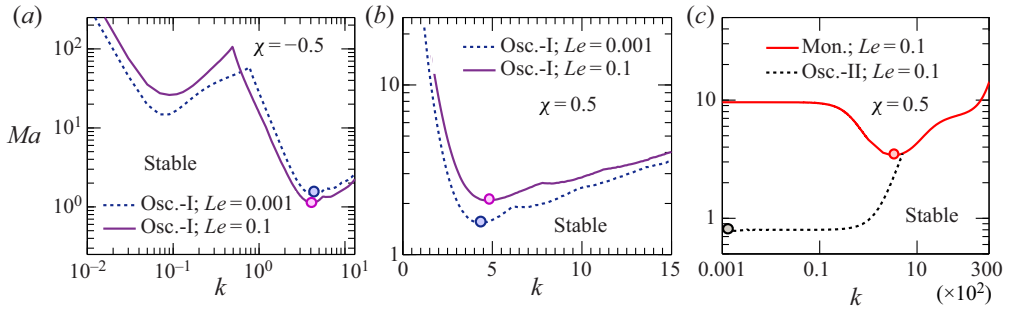


FIGURE 8. Effect of Lewis number  $Le$  on the monotonic and oscillatory instability threshold for (a,c)  $\chi < 0$  ( $= -0.5$ ) and (b)  $\chi > 0$  ( $= 0.5$ ). The dot (o) mark on each neutral curve represents the critical point of the curve. Panel (c) shows that, for a deformable surface at higher value of  $Le$ , a different type of long-wave oscillatory instability (oscillatory-II) can emerge in the fluid layer. Other parameters:  $Bi = 0.01$ ,  $De = 1$  and  $(Ga, \Sigma) = (0.1, 10^3)$ .

### 4.3. The role of thermal and solutal diffusivities

Let us now discuss the influence of thermal and solutal diffusivities on the onset of instability in the system. Here, we will demonstrate that, based on the diffusivity ratio  $Le$  ( $= D/\alpha$ ), a different kind of oscillatory instability (i.e. oscillatory-II) can emerge in the liquid layer. Before that, we first investigate the role played by  $Le$  on the emergence of oscillatory-I disturbances.

Figure 8(a) shows that an increased solute diffusivity corresponding to higher values of  $Le$  enhances the stability of the system against the long-wave oscillatory-I disturbances. This is due to the stabilizing role of solutocapillarity (see figure 6b) in producing this instability mode. Similarly, a destabilizing (stabilizing) solutocapillary force for  $\chi < 0$  ( $\chi > 0$ ) in the short-wave regime leads to a reduction (enhancement) in the stability threshold for higher solute diffusivity (compare figure 8a,b with figure 6b,c).

Figure 8(c) shows that, for a sufficiently large  $Le$  ( $\gtrsim O(10^{-2})$ ), the oscillatory-II disturbances can emerge in systems with a deformable free surface. Note that, at higher  $k$  values, the neutral curve for this particular instability mode (the dotted line) merges with the neutral curve for the monotonic mode (the solid line). This limits the appearance of oscillatory-II disturbances only in the long-wave form.

The other features of this instability mode are also quite different from those of the oscillatory-I mode. First, while the oscillatory-I instability can emerge in the system for the entire permissible range of model parameters, the oscillatory-II instability appears only in the case of a deformable free surface, for  $\chi > 0$  and  $Le \gtrsim O(10^{-2})$ . Although not shown here graphically, such disturbances get damped with the reducing deformability of the free surface and eventually disappear in a non-deformable free surface. Second, the oscillation frequency of the oscillatory-II mode is several orders of magnitude smaller than that of the oscillatory-I mode (see figure 9). This suggests that the oscillatory-II perturbations develop with a significantly large oscillation period compared to the oscillatory-I disturbances.

Now, in order to understand the physical mechanism behind the origination of the oscillatory-II disturbances and to elucidate the role of liquid elasticity on their onset, we plot in figure 10 the variation of  $Ma_c(\chi)$  with  $De$  for this instability mode. The disappearance of these disturbances for purely thermocapillary-driven convection ( $Ma_c \rightarrow \infty$  as  $\chi \rightarrow 0$ ) and the reduction of  $Ma_c$  with  $\chi$  suggest that the competition between

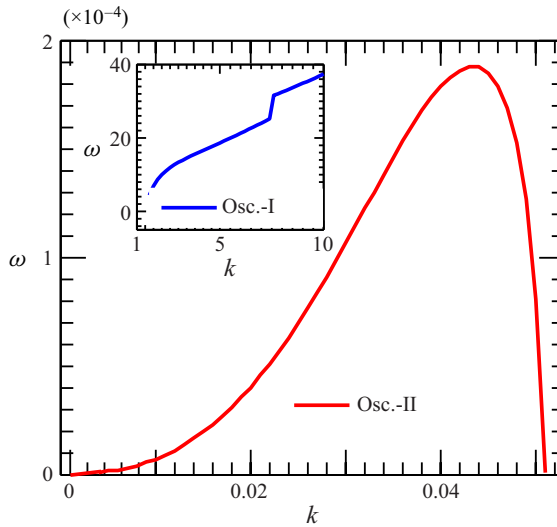


FIGURE 9. Comparison of the oscillation frequency of neutral perturbations for the oscillatory-II mode with oscillatory-I mode (shown in the inset). Parameters:  $\chi = 0.5$ ,  $Bi = 0.01$ ,  $De = 1$ ,  $Le = 0.1$  and  $(Ga, \Sigma) = (0.1, 10^3)$ .

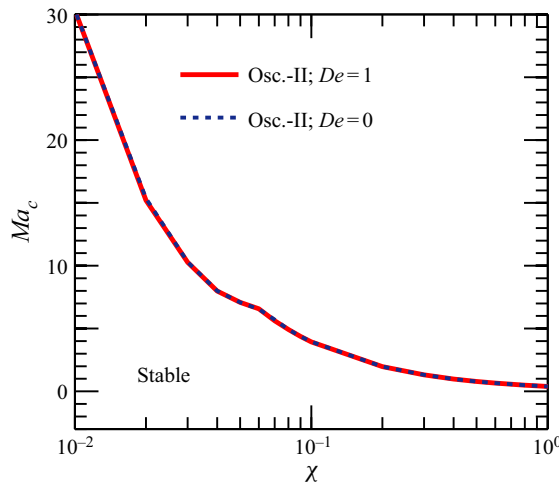


FIGURE 10. Variation of the critical Marangoni number  $Ma_c$  with  $\chi$  for the oscillatory-II mode at  $Bi = 0.01$ ,  $Le = 0.1$  and  $(Ga, \Sigma) = (0.1, 10^3)$ . Note that no oscillatory-II instability emerges for  $\chi \leq 0$ .

stabilizing thermocapillary and destabilizing solutocapillary forces gives rise to the oscillatory-II mode. A shorter mass diffusion time scale ( $H^2/D$ ) is here essential to overcome the stabilizing action of thermocapillarity by the destabilizing solutocapillary force. This explains the reason behind the emergence of oscillatory-II instability only for higher values of  $Le$  ( $= (H^2/\alpha)/(H^2/D) \gtrsim O(10^{-2})$ ). Another key observation from figure 10 is that the  $Ma_c(\chi)$  neutral curves for different values of  $De$  ( $= 0$  and  $1$ ) collapse onto a single curve. This implies that the stability threshold for the oscillatory-II mode is not affected by the elastic behaviour of the binary mixture.

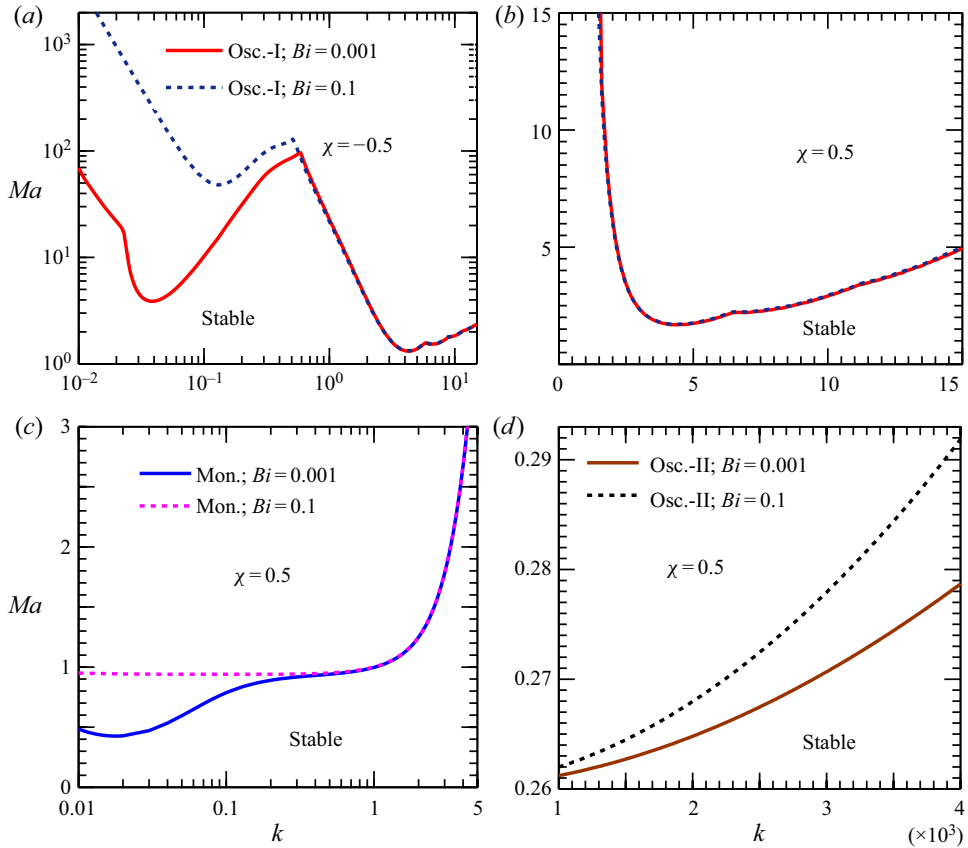


FIGURE 11. Effect of Biot number  $Bi$  on the monotonic and oscillatory instability threshold for (a)  $\chi < 0$  ( $= -0.5$ ), and (b,c,d)  $\chi > 0$  ( $= 0.5$ ) for a film with deformable free surface ( $Ga, \Sigma$ ) = (0.1,  $10^3$ ). Other parameters:  $De = 1$  and  $Le = 0.01$ .

4.4. The role of heat transfer rate at the free surface

Lastly, we discuss the role of the Biot number on the stability threshold of the system. In figure 11, the neutral stability curves for each instability mode are plotted for two different values of  $Bi$  ( $= 10^{-3}$  and 0.1). It turns out that, at higher values of  $Bi$ , the enhanced heat transfer rate from the free surface increases the stability of the system against the long-wave disturbances (see figure 11(a,c,d) at small  $k$ ). However, the influence of  $Bi$  is less significant in the short-wave regime, as reflected by the saturation of curves in this regime (see figure 11(a-c) at large  $k$ ). The magnitude of  $Bi$ , therefore, bears significant importance in the emergence of long-wave instability in the liquid layer.

5. Spatial structure of eigenvectors at neutral stability

We now briefly examine the effect of elasticity on the spatial structure of eigenvectors  $\hat{\psi}$ ,  $\hat{\theta}$  and  $\hat{c}$  at the neutral stability boundary. Figure 12 plots the normalized spatial profiles of  $\hat{\psi}$  for each instability mode at two different levels of elasticity ( $De = 0$  and 1) of the binary mixture.

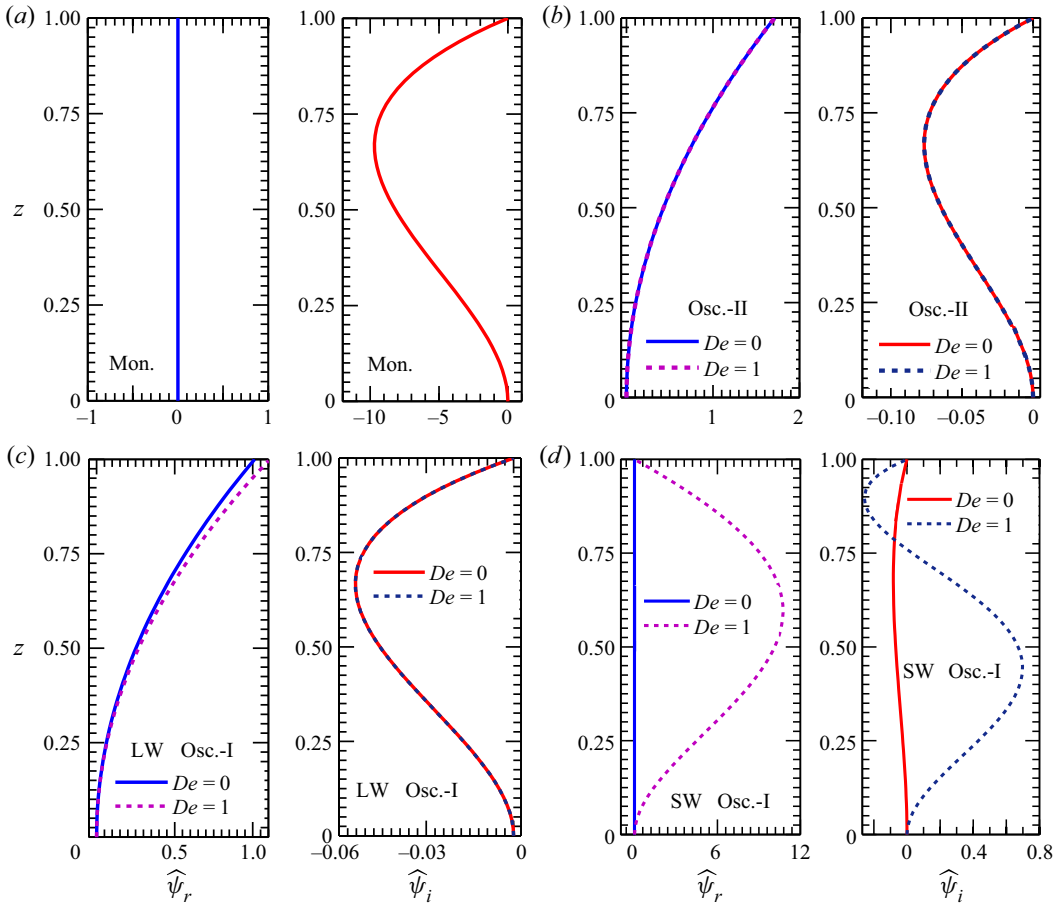


FIGURE 12. Effect of liquid elasticity on the eigenvector  $\hat{\psi}$  profiles (normalized) at the neutral stability boundary for (a) monotonic mode, (b) oscillatory-II mode, (c) long-wave oscillatory-I mode and (d) short-wave oscillatory-I mode. Profiles in panels (a,b) correspond to the critical point of the respective neutral curve presented in figure 8(a). Profiles in panels (c,d) refer to the critical point of the long-wave and short-wave branches of the neutral curves depicted in figure 4(a). The eigenvectors are plotted for a deformable free surface  $(Ga, \Sigma) = (0.1, 10^3)$ .

Note that  $\hat{\psi}$  ( $= \hat{\psi}_r + i\hat{\psi}_i$ ) is a complex-valued eigenvector. For the monotonic instability mode,  $\hat{\psi}_r = 0$ , and thus  $\hat{\psi}$  ( $= i\hat{\psi}_i$ ) assumes a purely imaginary value (see figure 12a). Similarly to the monotonic instability threshold, the spatial structure of  $\hat{\psi}$  also remains independent of the elasticity of the mixture. For the oscillatory-II as well as the long-wave oscillatory-I mode, figure 12(b,c) demonstrate that the spatial structures of  $\hat{\psi}$  are identical and essentially remain unaltered by the elasticity of the liquid. This observation is also consistent with the results obtained in § 4 (which suggest that the onset of long-wave oscillatory disturbances get least affected by the elastic behaviour of the binary mixture). On the other hand, the spatial shape of  $\hat{\psi}$  for the short-wave oscillatory-I mode is found to be highly sensitive to the liquid elasticity (see figure 12d).

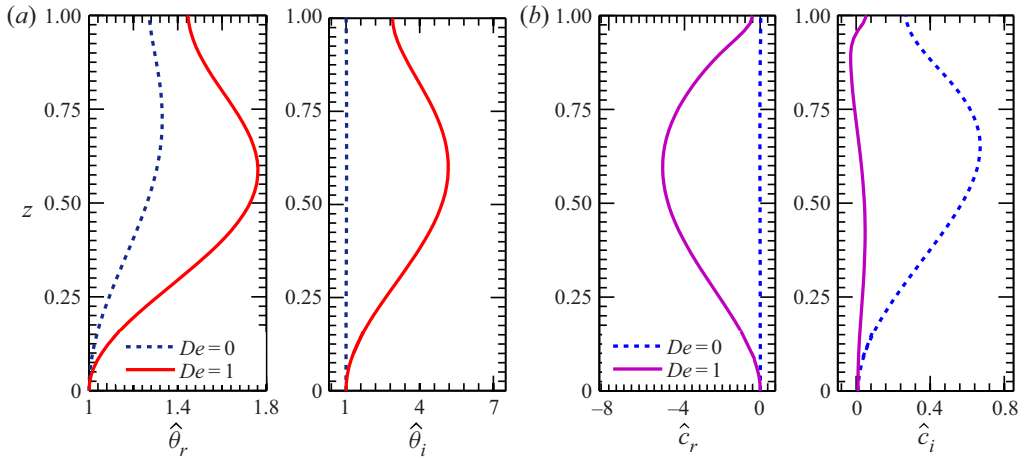


FIGURE 13. Effect of elasticity on the spatial profiles of (a) temperature  $\hat{\theta}$  and (b) concentration  $\hat{c}$  eigenvectors (normalized) at the neutral stability point. Profiles for each  $De$  in panels (a,b) correspond to the critical point of the short-wave oscillatory-I branch presented in figure 4(a).

Here  $\hat{\psi}$  exhibits substantial spatial distortions, with sharp gradients for higher values of  $De$ , yielding more complicated structures.

The spatial structures of eigenvectors  $\hat{\theta} (= \hat{\theta}_r + i\hat{\theta}_i)$  and  $\hat{c} (= \hat{c}_r + i\hat{c}_i)$  for the short-wave oscillatory-I mode are presented in figure 13. Clearly, both eigenvectors demonstrate more distorted spatial structures for an increasing level of elasticity of the mixture.

We can, therefore, conclude that, except for the short-wave oscillatory-I mode, the spatial structure of eigenvectors for the remaining instability modes is not influenced by the elastic behaviour of the liquid.

### 6. An approximate model

In this section, we derive an approximate model by performing a long-wave asymptotic expansion of the EVP (3.12)–(3.14) and rescaling the parameters ( $Bi, De, \Sigma$ ). This model can be helpful in getting a qualitative insight into the stability picture without numerically solving the problem.

In the long-wavelength limit, given the very small ratio between mean film thickness  $H$  and disturbance wavelength  $\ell$  (i.e.  $\varepsilon = H/\ell \ll 1$ ), the horizontal variations evolve much more slowly compared to the vertical ones. Here, we can apply the lubrication approximation, consisting of slow longitudinal  $X \sim \varepsilon x$  and temporal  $T \sim \varepsilon^2 t$  variables. We, therefore, proceed by introducing the following scaling for  $k$  and  $\lambda$ :

$$k = \varepsilon q, \quad \lambda = \varepsilon^2 \lambda_o. \tag{6.1a,b}$$

Furthermore, for this analysis, we rescale the parameters  $Bi, De$  and  $\Sigma$  as

$$Bi = \varepsilon^2 \mathcal{B}, \quad De = \varepsilon^{-2} De, \quad \Sigma = \varepsilon^{-2} Ca. \tag{6.2a-c}$$

Scaling (6.2) suggests that the proposed model remains effective only for small values of  $Bi$  and large  $De$  and  $\Sigma$ . Recall that a small  $Bi$  physically represents a poorly conducting

free surface, while large  $De$  signifies a highly viscoelastic liquid. It is important to note that, owing to the weak influence of elasticity on the long-wave instability threshold (see figures 4 and 10), the projected model would be able to predict the stability margin in the long-wave regime even for small values of  $De$  (graphically demonstrated a little later). The scaling (6.2*b*) will only help in better predicting the stability boundary in the short-wave regime at higher values of  $De$  (surpassing the approximations made in (6.1)). Furthermore, the consideration of large  $\Sigma$  is well justified here since its magnitude is usually high. However, we do not impose any restrictions on the magnitude of other dimensionless parameters, and they remain at  $O(1)$  with respect to  $\varepsilon$ .

The perturbation fields are now expanded for  $\varepsilon$  as follows:

$$\left. \begin{aligned} \widehat{\psi} &= \varepsilon\psi_o + \varepsilon^3\psi_2 + \dots, & \widehat{\theta} &= T_o + \varepsilon^2T_2 + \dots, & \widehat{c} &= c_o + \varepsilon^2c_2 + \dots, \\ \widehat{\xi} &= \xi_o + \varepsilon^2\xi_2 + \dots. \end{aligned} \right\} \quad (6.3a-d)$$

Introducing the rescaled parameters and expansions (6.1)–(6.3) into the EVP (3.12)–(3.14), we first collect the terms with identical order in  $\varepsilon$ . At the leading order, the governing equations (3.12*a–c*) simplify to

$$\frac{d^4\psi_o}{dz^4} = 0, \quad \frac{d^2T_o}{dz^2} = 0, \quad \frac{d^2c_o}{dz^2} = 0; \quad (6.4a-c)$$

and are accompanied by the following set of boundary conditions:

$$\psi_o = 0, \quad \frac{d\psi_o}{dz} = 0, \quad \frac{dT_o}{dz} = 0, \quad \frac{dc_o}{dz} = 0 \quad \text{at } z = 0, \quad (6.5a-d)$$

$$iq\psi_o = \lambda_o\xi_o, \quad \frac{dT_o}{dz} = 0, \quad \frac{dc_o}{dz} = 0, \quad (6.6a-c)$$

$$\frac{d^3\psi_o}{dz^3} = iq\xi_o(Ga + Caq^2)(1 - \lambda_oDe), \quad (6.6d)$$

$$\frac{d^2\psi_o}{dz^2} = iqMa(1 - \lambda_oDe)(c_o - T_o + \xi_o + \chi\xi_o) \quad \text{at } z = 1. \quad (6.6e)$$

The solutions to BVP (6.4)–(6.6) is given by

$$\psi_o = \frac{i\xi_o}{6q}[q^2(Ga + Caq^2)(1 - \lambda_oDe)(z^3 - z^2) - 6\lambda_oz^2], \quad T_o = \mathcal{J}, \quad c_o = \varphi, \quad (6.7a-c)$$

where  $\mathcal{J}$  and  $\varphi$  are constants yet to be determined.

At the second order with respect to  $\varepsilon$ , only the energy and mass balance equations find relevance. They read

$$\frac{d^2T_2}{dz^2} + (\lambda_o - q^2)T_o = iq\psi_o, \quad (6.8a)$$

$$Le\frac{d^2c_2}{dz^2} + (\lambda_o - Leq^2)c_o = -i\chi(1 + Le)q\psi_o + Le\chi\lambda_oT_o. \quad (6.8b)$$

The associated boundary conditions (3.13c,d) and (3.14b,c) now take the following form:

$$\frac{dT_2}{dz} = 0, \quad \frac{dc_2}{dz} = 0 \quad \text{at } z = 0, \tag{6.9a,b}$$

$$\frac{dT_2}{dz} = -\mathcal{B}(T_o - \xi_o), \quad \frac{dc_2}{dz} = \chi \mathcal{B}(T_o - \xi_o) \quad \text{at } z = 1. \tag{6.10a,b}$$

Integrating (6.8a,b) across the film  $0 \leq z \leq 1$  and incorporating the boundary conditions (6.9) and (6.10), we obtain

$$\xi_o = \frac{72(\phi + q^2)}{72\mathcal{B} - 24\lambda_o - \mathcal{G}\mathcal{Q}q^2} \mathcal{J}, \tag{6.11}$$

$$\varphi = \frac{\chi \phi (72\mathcal{B} - 24\lambda_o - \mathcal{G}\mathcal{Q}q^2) + [\chi(1 + Le^{-1})(24\lambda_o + \mathcal{G}\mathcal{Q}q^2) - 72\mathcal{B}\chi](\phi + q^2)}{(72\mathcal{B} - 24\lambda_o - \mathcal{G}\mathcal{Q}q^2)(q^2 - \lambda_o Le^{-1})} \mathcal{J}, \tag{6.12}$$

where  $\phi = \mathcal{B} - \lambda_o$ ,  $\mathcal{G} = (1 - \lambda_o \mathcal{D}e)$  and  $\mathcal{Q} = Ga + Caq^2$ .

Finally, the substitution of  $\xi_o$  and  $\varphi$  into the tangential stress balance boundary condition (6.6e) yields the following sought expression for  $Ma$ :

$$Ma = \frac{24 \mathcal{N}_0 + \lambda_o \mathcal{N}_1 + \lambda_o^2 \mathcal{N}_2 + \lambda_o^3 \mathcal{N}_3}{q^2 \mathcal{D}_0 + \lambda_o \mathcal{D}_1 + \lambda_o^2 \mathcal{D}_2 + \lambda_o^3 \mathcal{D}_3}; \tag{6.13}$$

the coefficients  $\mathcal{N}_j$  and  $\mathcal{D}_j$  ( $j = 0-3$ ) are defined in [appendix A](#).

Equation (6.13) governs the stability threshold for both the monotonic and oscillatory disturbances within the approximations made in (6.1) and (6.2). The validity bound for this analysis will be discussed in the forthcoming subsections. An inspection of (6.13) reveals that, in accordance with the numerical results presented in § 4, the stability threshold for both the instability modes are independent of  $Pr$ .

### 6.1. Monotonic mode

Let us start with the case of monotonic instability. Substitution of  $\lambda_o = 0$  into (6.13) yields the explicit expression for the neutral stability curve of this instability mode:

$$Ma_{mon.} = \frac{48Le\mathcal{Q}(\mathcal{B} + q^2)}{\mathcal{B}\chi \mathcal{Q} + [\mathcal{Q}\chi + Le(72 + \mathcal{Q})(1 + \chi)]q^2}. \tag{6.14}$$

Returning to the unscaled parameters  $k$ ,  $Bi$  and  $\Sigma$ , we get

$$Ma_{mon.} = \frac{48Le(Ga + \Sigma k^2)(Bi + k^2)}{Bi\chi(Ga + \Sigma k^2) + [\chi(Ga + \Sigma k^2) + Le(1 + \chi)(72 + Ga + \Sigma k^2)]k^2}. \tag{6.15}$$

Equation (6.15) depicts the stability boundary for a system with deformable free surface. For a non-deformable surface (i.e. in the limit  $(Ga + \Sigma k^2) \rightarrow \infty$ ), the stability margin



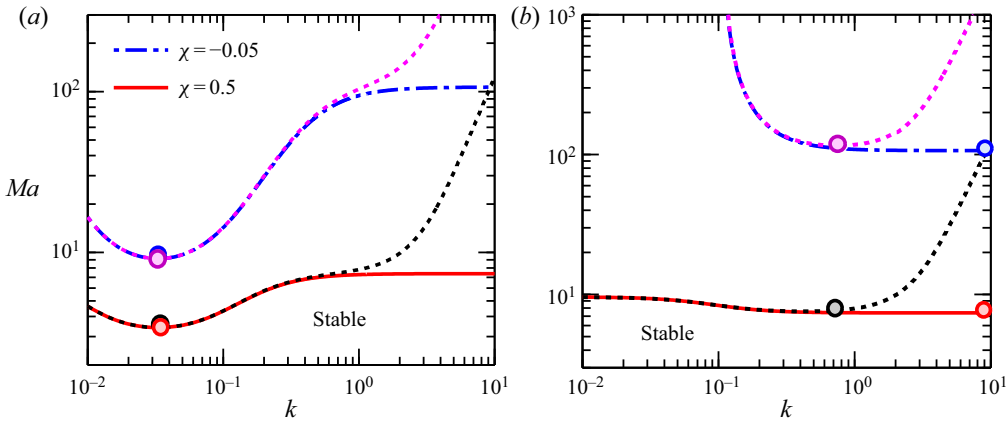


FIGURE 14. Comparison of results obtained from the approximate model (solid and dash-dotted lines) with the numerical results (dotted lines) for the monotonic instability mode via the neutral stability curve (a) deformable surface  $(Ga, \Sigma) = (0.1, 10^3)$ , and (b) non-deformable surface  $(Ga, \Sigma) \rightarrow \infty$ . The dot (o) mark on each neutral curve represents the critical point of the curve. Other parameters:  $Bi = 0.01$  and  $Le = 0.1$ .

(6.15) becomes

$$Ma_{mon.} = \frac{48Le(Bi + k^2)}{Bi\chi + (Le + \chi + Le\chi)k^2}. \tag{6.16}$$

The minimization of (6.15) for  $Ma$  now yields the following expression for critical wavenumber  $k_c$ :

$$k_c = \sqrt{\frac{BiGa\Sigma + \sqrt{72BiGa\Sigma(72 + Ga - Bi\Sigma)}}{\Sigma(72 - Bi\Sigma)}} \quad \text{for } \chi \neq -1. \tag{6.17}$$

Interestingly, (6.17) also indicates the domain of validity of this approximate model. Note that, for  $Bi\Sigma = 72$ , one has  $k_c \rightarrow \infty$ , violating the lubrication approximation,  $k \ll 1$ . Therefore, the proposed model holds good only for  $Bi\Sigma < 72$ . This event is graphically demonstrated in figure 14. One can readily see that the critical parameters  $(Ma_c, k_c)$  predicted by the long-wave theory agree with the numerical results only for  $Bi\Sigma = 10 (< 72)$  (i.e. for a deformable free surface, see figure 14a).

Equations (6.15) and (6.16) indicate that, at  $k \rightarrow \infty$ , irrespective of the deformability of the free surface,  $Ma$  attains the limiting value

$$Ma_{mon.,k \rightarrow \infty} = \frac{48Le}{Le + \chi + Le\chi}. \tag{6.18}$$

It should be noted that, for  $Bi\Sigma \geq 72$ ,  $Ma \rightarrow Ma_c$  in (6.18). However, this  $Ma_c$  has lost the quantitative agreement with the numerical results owing to the violation of the long-wave approximation (compare panels figure 14a,b).

From (6.15) and (6.16) it further follows that, for  $k \in [0, \infty)$ , irrespective of the deformability of the free surface,  $Ma$  remains positive for  $\chi > 0$  and becomes negative when  $\chi < -Le/(1 + Le)$ . Hence, there must be a discontinuity in the neutral curves in the domain  $0 > \chi > -Le/(1 + Le)$ , suggesting the emergence of instability for heating

from the top as well as from below. For the case of a deformable free surface, this point of discontinuity ( $k_d$ ) is given by the real and positive root of

$$\gamma_0 k_d^4 + \gamma_1 k_d^2 + \gamma_2 = 0; \tag{6.19}$$

the coefficients  $\gamma_j$  ( $j = 0-2$ ) are presented in [appendix B](#).

On the other hand, for a non-deformable surface, the point of discontinuity ( $k_d^{nd}$ ) lies at

$$k_d^{nd} = \sqrt{-\frac{Bi\chi}{Le + \chi + Le\chi}}. \tag{6.20}$$

Thus, for  $\chi \in (0, -Le/(1 + Le))$ , the monotonic instability sets in for heating the liquid layer from below with  $k > k_d$  (or  $k_d^{nd}$  for a non-deformable surface) and *vice versa*. For the parameter values  $(Le, \chi) = (0.1, -0.05)$  this situation is graphically illustrated in [figure 14](#). Here,  $k_d = 2.8 \times 10^{-3}$  and  $k_d^{nd} = 0.105$  (see [figure 14a,b](#)). A comprehensive study of the stability characteristics of the branch pertaining to the negative values of  $Ma$  is beyond the scope of this paper.

Finally, a few previously reported results in the literature can be derived from the expressions (6.15) and (6.16). Since the monotonic instability threshold remains unaffected by the elastic behaviour of the liquid, therefore, in the limit  $\chi = 0$ , (6.15) yields the results for purely thermocapillary-driven convection in a Newtonian liquid layer (Shklyaev, Alabuzhev & Khenner 2012). For such a film, (6.16) yields the well-known asymptotic value  $Ma_{mon.} = 48$  in the limit  $(Ga, \Sigma) \rightarrow \infty$ , for either  $Bi = 0$  or  $k \rightarrow \infty$  (Pearson 1958).

### 6.2. Oscillatory mode

The stability threshold for this instability mode is obtained by substituting  $\lambda_o = i\omega$  in (6.13). This yields

$$Ma_{\pm osc.} = \frac{(\mathcal{N}_0 - \omega_{\pm}^2 \mathcal{N}_2)(\mathcal{D}_0 - \omega_{\pm}^2 \mathcal{D}_2) + \omega_{\pm}^2 (\mathcal{N}_1 - \omega_{\pm}^2 \mathcal{N}_3)(\mathcal{D}_1 - \omega_{\pm}^2 \mathcal{D}_3)}{(\mathcal{D}_0 - \omega_{\pm}^2 \mathcal{D}_2)^2 + \omega_{\pm}^2 (\mathcal{D}_1 - \omega_{\pm}^2 \mathcal{D}_3)^2}, \tag{6.21}$$

where  $\omega_{\pm} = (\omega_+, \omega_-)$  are the oscillation frequencies for  $Ma_{\pm osc.} = (Ma_{+osc.}, Ma_{-osc.})$ , respectively, and are given by

$$\omega_{\pm}^2 = \frac{1}{2(\mathcal{N}_3 \mathcal{D}_2 - \mathcal{N}_2 \mathcal{D}_3)} [(\mathcal{N}_1 \mathcal{D}_2 + \mathcal{N}_3 \mathcal{D}_0 - \mathcal{N}_2 \mathcal{D}_1 - \mathcal{N}_0 \mathcal{D}_3) \pm \sqrt{(\mathcal{N}_2 \mathcal{D}_1 + \mathcal{N}_0 \mathcal{D}_3 - \mathcal{N}_1 \mathcal{D}_2 - \mathcal{N}_3 \mathcal{D}_0)^2 - 4(\mathcal{N}_3 \mathcal{D}_2 - \mathcal{N}_2 \mathcal{D}_3)(\mathcal{N}_1 \mathcal{D}_0 - \mathcal{N}_2 \mathcal{D}_3)}]. \tag{6.22}$$

Note that  $\omega_{\pm}^2$  ( $\omega_{\pm}^2$ ) refers to the oscillation frequency obtained from adding (subtracting) the square root terms in the numerator of (6.22). For a given set of model parameters  $(\mathcal{B}, Ca, De, Ga, Le, \chi)$ , the presence of two different oscillation frequencies (i.e.  $\omega_+$  and  $\omega_-$ ) suggests the possible emergence of two different oscillatory instabilities in the system (namely, oscillatory-I and oscillatory-II, as discussed in § 4). Confirming the numerical results, one of the oscillation frequencies vanishes for a non-deformable surface (must be

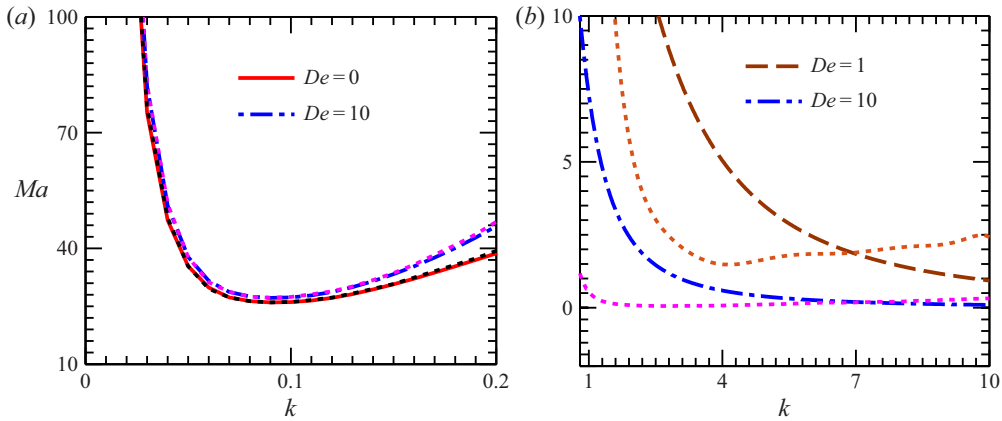


FIGURE 15. Comparison between results of the numerical computation (dotted lines) and the approximate model (solid and dash-dotted lines) for the oscillatory-I mode via neutral stability curve: (a) long-wave branch at  $Le = 0.1$ ,  $\chi = -0.5$ ; and (b) short-wave branch at  $Le = 10^{-3}$ ,  $\chi = 0.5$ . Other parameters:  $Bi = 0.01$  and  $(Ga, \Sigma) = (0.1, 10^3)$ .

the one related with the oscillatory-II mode), for which the expressions of the neutral curve and oscillation frequency are given by

$$Ma_{osc.} = \frac{48(Bi + k^2 + Lek^2)}{[(1 + DeLek^2) + \chi(1 + BiDe + Dek^2 + DeLek^2)]k^2} \tag{6.23}$$

and

$$\omega^2 = \frac{\mathcal{L}_0k^6 + \mathcal{L}_1k^4 + \mathcal{L}_2k^2 + \mathcal{L}_3}{\mathcal{L}_4k^2 + \mathcal{L}_5}, \tag{6.24}$$

respectively. The coefficients  $\mathcal{L}_j$  ( $j = 0-5$ ) are defined in appendix C. It is worth noting that, in the limit  $De = 0$ , (6.23) matches with the results for a Newtonian liquid (Podolny *et al.* 2005).

Given the convoluted form of the neutral curves (6.21) and (6.23), any further analytical progress in estimating their validity bound now becomes a rather intricate task. Thus, we verify the accuracy of this analysis by comparing the results with numerical computations for a wide range of the parameters ( $De, Le, \chi$ ) within the limit  $Bi\Sigma < 72$ . For the long-wave branch of oscillatory-I mode, figure 15(a) shows that the results obtained from the approximate model agree with the numerical results in an excellent manner for both the Newtonian ( $De = 0$ ) and highly viscoelastic ( $De = 10$ ) binary mixtures. Here, the oscillation frequency is given by  $\omega_-$ . However, this agreement is found to be poor for the short-wave branch, due to the violation of the lubrication approximation (see figure 15b). Nevertheless, the scaling adopted for  $De$  (see 6.2b) helps in achieving a qualitative agreement at higher values of  $De$ . The oscillation frequency for this branch is given by  $\omega_+$ .

Finally, this approximate model also predicts the emergence of oscillatory-II instability in the system. The oscillation frequency for this mode is given by  $\omega_-$ . Figure 16 shows that the developed model is capable of depicting the stability threshold in a fairly accurate manner for this instability mode as well.

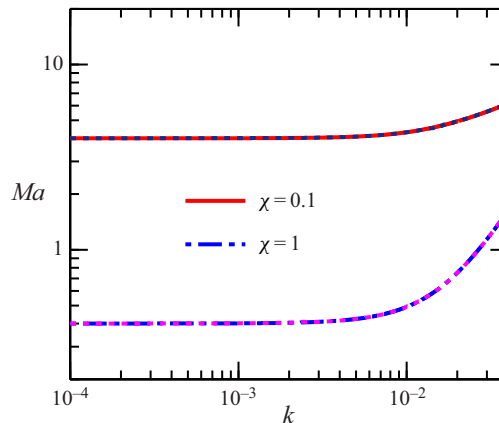


FIGURE 16. Comparison of results obtained from the approximate model (solid and dash-dotted lines) with the numerical results (dotted lines) for the oscillatory-II mode via the neutral stability curve at  $Bi = 0.01$ ,  $De = 1$ ,  $Le = 0.1$  and  $(Ga, \Sigma) = (0.1, 10^3)$ .

## 7. Phase diagrams

We have now understood that both monotonic and oscillatory instabilities can emerge in the present system (in either the long-wave or short-wave mode) depending on the values of the model parameters. The purpose of this section is to explore the parameter regions for each instability mode, wherein it becomes dominant in the liquid layer. The phase diagrams displayed in figure 17 are expected to be helpful for carrying out an experimental investigation of the present problem, especially in situations where one is interested in observing the convective patterns of a particular instability mode. Note that, since we are studying here the stability characteristics of a viscoelastic film incorporating the Soret effect, the phase diagrams are plotted in the  $\chi - De$  plane. In an effort to identify the region of dominance for each instability mode, the parameter set  $(Ga, \Sigma, Le)$  is varied to take into account the surface deformability with weak/strong solute diffusivity. However, we hold the parameters  $Bi (= 0.01)$  and  $Pr (= 10)$  fixed. In figure 17(a-d), region 1 stands for the monotonic mode, region 2 for the long-wave oscillatory-I mode, region 3 for the short-wave oscillatory-I mode, and region 4 for the oscillatory-II mode. An important point that needs to be highlighted here is that a dataset in  $(\chi, De)$  corresponding to the boundary between adjacent instability modes refers to a competition between them to become the dominant instability mode in the system. Such interaction between the instability modes may lead to the formation of convective patterns, which will be significantly different from the patterns that appear far from this location.

For a liquid layer with a deformable free surface, figure 17(a,b) plot the phase diagrams for two different values of  $Le$ :  $Le = 10^{-3}$  and 0.1, respectively. Figure 17(a) shows that, in the weakly viscoelastic regime (i.e.  $De \lesssim 0.1$ ), the long-wave oscillatory-I mode (region 2) becomes dominant for  $\chi < 0$ . The characteristics of this mode are identical for both the Newtonian and viscoelastic binary mixtures, as we have learned from § 4.1. However, in the highly elastic regime (i.e. for  $De > 0.1$ ), this long-wave mode is replaced by its short-wave counterpart (region 3). Since the onset of this particular instability mode is triggered by the elasticity of the mixture (but weakly dominated by the solutocapillary force), the short-wave oscillatory-I mode can become dominant even for  $\chi > 0$  at higher values of  $De$ . Except for such larger values of  $De$ , the monotonic instability (region 1)

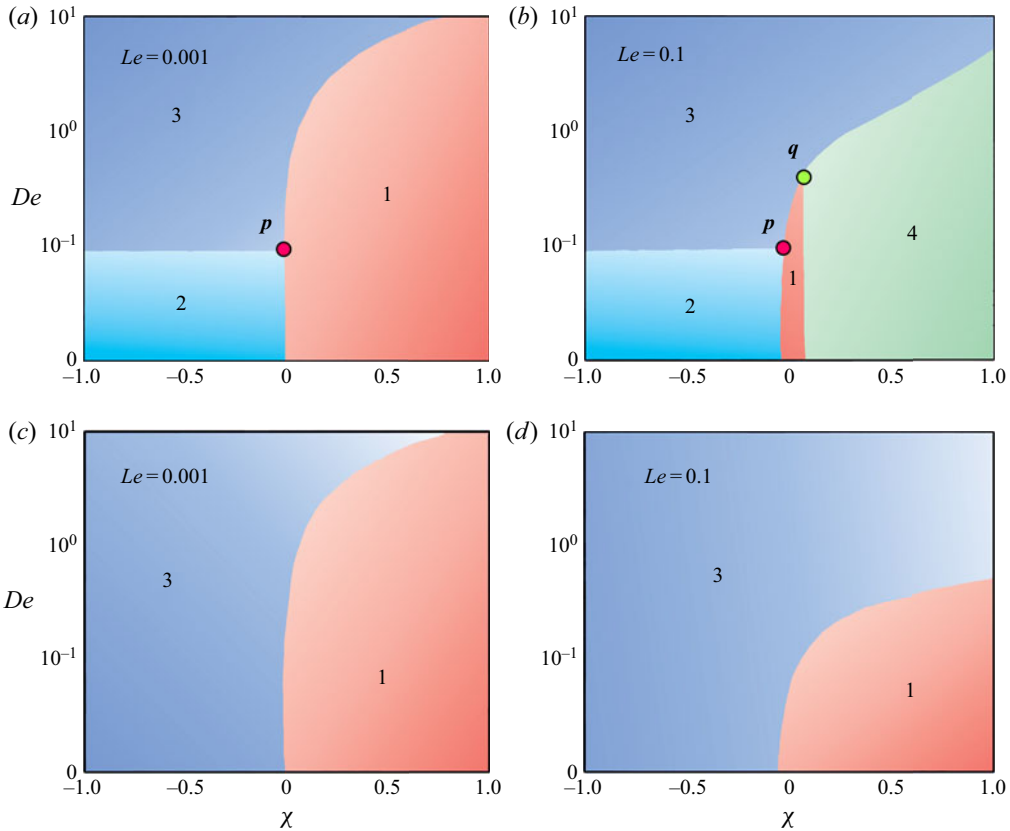


FIGURE 17. Phase diagrams for  $(\chi, De)$  at different  $Le$  enclosing the regimes of dominant instability mode: (a,b) deformable free surface  $(Ga, \Sigma) = (0.1, 10^3)$ , and (c,d) non-deformable free surface  $(Ga, \Sigma) \rightarrow \infty$  at  $Bi = 0.01, Pr = 10$ . In all panels: regime 1, monotonic instability; regime 2, long-wave oscillatory-I instability; regime 3, short-wave oscillatory-I instability; and regime 4, oscillatory-II instability. At the points marked  $p$  and  $q$  in panels (a,b), the three adjacent instability modes can coexist.

prevails in the system for  $\chi > 0$  as well as for a narrow interval of  $\chi < 0$  (as discussed in § 6.1).

A comparison between figure 17(a) and (b) now reveals that, for a viscoelastic mixture with higher solute diffusivity ( $Le = 0.1$ ), the region of dominant monotonic instability shrinks drastically, and the oscillatory-II instability (region 4) emerges in the system for  $\chi > 0$ . Furthermore, region 1 shifts slightly towards the left (due to the widening of the range  $\chi \in (0, -Le/(Le + 1))$ ; see § 6.1), and region 3 expands towards the right. However, the transition boundary between the long-wave oscillatory-I (region 2) and short-wave oscillatory-I (region 3) mode remains unaltered by the value of  $Le$ . Another key observation from figure 17(a,b) is that, for  $(\chi, De)$  values corresponding to the points  $p$  and  $q$  in panels (a,b), three different instability modes, *viz.* monotonic : long-wave oscillatory-I : short-wave oscillatory-I and monotonic : long-wave oscillatory-II : short-wave oscillatory-I, respectively, can compete together in the system.

For a non-deformable free surface, figure 17(c,d) demonstrate that, irrespective of the diffusivity ratio  $Le$ , the conductive state bifurcates either to the monotonic (region 1) or

the short-wave oscillatory-I (region 3) mode depending on the parameter set  $(\chi, De)$ . It should be noted that the long-wave oscillatory mode (both oscillatory-I and oscillatory-II) cannot become the dominant instability mode here (due to the dampening out of such perturbations by the increased gravitational and surface tension forces).

Thus, [figure 17\(a–d\)](#) provide a comprehensive review of the stability picture under the parameter space  $(De, \chi, Le, Ga, \Sigma)$ . Besides exploring the parameter regions for which a particular instability mode becomes dominant in the system, they also highlight the competition between the various instability modes that may occur based upon a few specific parameter sets. We expect these phase diagrams to provide valuable guidance in choosing the parameters set for a realistic experimental set-up.

## 8. Summary and conclusions

In this work, we have investigated the Marangoni instability problem for a thin viscoelastic film confined between its deformable free surface and a flat rigid substrate. The novelty of this analysis lies in considering the binary aspect of the liquid, along with the incorporation of the Soret effect. Linear stability analysis performed around a quiescent basic state reveals that thermosolutocapillarity, in the presence of Soret diffusion, shows an entirely different stability picture from that for purely thermocapillary-driven convection (Sarma & Mondal 2019). For the system subjected to heating from below, it is found that, apart from the monotonic instability, two different oscillatory instabilities, namely oscillatory-I and oscillatory-II, can emerge in the system depending on the physical situations governed by the parameter space  $(Bi, De, Le, \chi, Ga, \Sigma)$  (see [figure 17](#)).

The monotonic instability threshold remains unaffected by the elastic behaviour of the mixture, resulting in identical stability characteristics for both the Newtonian and viscoelastic liquid films. However, the instability mode that draws particular attention in the context of Marangoni convection in a viscoelastic film is the oscillatory instability mode. The oscillatory-I instability may appear in either the long-wave or short-wavelength form depending on the deformability of the free surface and the elasticity level of the liquid. It is found that, while the short-wave oscillatory-I mode is more universal, the long-wave oscillatory-I mode can also become dominant in a weakly viscoelastic film ( $De \lesssim 0.1$ ) with deformable free surface for  $\chi < 0$ . The oscillatory-II mode is more case-specific and is likely to emerge in a binary liquid film (irrespective of the elasticity of the mixture) having a deformable free surface at higher solute diffusivity  $Le \gtrsim O(10^{-2})$  and for  $\chi > 0$ . It is a long-wavelength instability that appears with significantly large oscillation period compared to the oscillatory-I mode.

This leads to the following main conclusions from this study: the solutocapillary effect plays a crucial role only in the case of long-wave disturbances. For  $\chi > 0$  (or equivalently  $S > 0$ ), solutocapillarity causes the appearance of long-wave monotonic or oscillatory-II instability (depending on the diffusivity ratio  $Le$ ), whereas for  $\chi < 0$ , it enhances the stability of the system against the long-wave oscillatory-I perturbations. On the other hand, the thermocapillary effect is primarily responsible for the short-wave oscillatory-I disturbances. The solutocapillarity plays here a minor role. Triggered by the elasticity of the mixture, the short-wave oscillatory-I instability can, therefore, appear for any  $\chi \in \mathbb{R}$ . While the increased (convective) heat transfer rate and the reduced deformability of the free surface enhance the stability of the system against long-wave perturbations, the increasing elasticity of the liquid makes the system more vulnerable towards short-wave disturbances.

However, the conditions (*viz.* the film thickness, the temperature difference across the film, the corresponding size of the convection cell and its oscillation period) at which one may experimentally observe a particular instability mode detected in this study remain unclear. This is primarily due to uncertainty over the data related to physical properties of the liquid, especially the Soret coefficient  $S$  and the relaxation time  $\lambda$ , which change with the composition of the liquid. Separate experimentation is needed for this purpose. Nevertheless, provided with a prior estimation of the parameters ( $\lambda, S$ ), the present analysis can be helpful in predicting the instability modes as soon as a bifurcation of the conductive base state occurs. Further experimental and theoretical investigations are thus necessary to understand the pattern dynamics in the post-critical regime for the present convection phenomenon. It is also worth extending the present model to study an unsteady problem, e.g. evaporative Marangoni convection (Doumenc *et al.* 2010; Pillai & Narayanan 2018) in a polymeric film, or to develop a coupled film–substrate model (Batson *et al.* 2019) to analyse the convection phenomenon for more complex systems.

### Acknowledgements

The authors are grateful to the referees for their valuable comments and suggestions that significantly improved the manuscript. They would also like to acknowledge the computing facilities available at the Microfluidics and Microscale Transport Process Laboratory, IIT Guwahati, where this work was carried out.

### Declaration of interests

The authors report no conflict of interest.

### Appendix A. Expressions for the coefficients used in (6.13)

The coefficients of (6.13) are as follows:

$$\mathcal{N}_0 = 2BQq^4 + 2Qq^6, \quad (\text{A } 1)$$

$$\mathcal{N}_1 = -2B(3 + QLe^{-1})q^2 - 2[3 + Q(1 + Le^{-1} + BDe)]q^4 - 2DeQq^6, \quad (\text{A } 2)$$

$$\mathcal{N}_2 = 6BLe^{-1} + 2[(3 + Q + BDeQ)Le^{-1} + 3]q^2 + 2DeQ(1 + Le^{-1})q^4, \quad (\text{A } 3)$$

$$\mathcal{N}_3 = -6Le^{-1} - 2DeQLe^{-1}q^2; \quad (\text{A } 4)$$

$$D_0 = BQ\chi Le^{-1}q^2 + [(1 + \chi)(72 + Q) + Q\chi Le^{-1}]q^4, \quad (\text{A } 5)$$

$$D_1 = -48B\chi Le^{-1} - [(1 + \chi)(48 + QLe^{-1}) + 2(36 + 24\chi + De\chi Q)Le^{-1}]q^2 - 2De[Q\chi Le^{-1} + (1 + \chi)(36 + Q)]q^4, \quad (\text{A } 6)$$

$$D_2 = 48(1 + \chi + BDe\chi)Le^{-1} + De^2Q(1 + \chi + \chi Le^{-1})q^4 + De[2(1 + \chi)(24 + QLe^{-1}) + (72 + 48\chi + BDe\chi Q)Le^{-1}]q^2, \quad (\text{A } 7)$$

$$D_3 = -De(1 + \chi)(48 + DeQq^2)Le^{-1}. \quad (\text{A } 8)$$

Recall that  $Q = Ga + Caq^2$ .

**Appendix B. Expressions for the coefficients utilized in (6.19)**

The expressions for the coefficients of (6.19) are given below:

$$\gamma_0 = \Sigma(Le + \chi + Le\chi), \quad (\text{B } 1)$$

$$\gamma_1 = \chi(Ga + Bi\Sigma) + Le(1 + \chi)(72 + Ga), \quad (\text{B } 2)$$

$$\gamma_2 = BiGa\chi. \quad (\text{B } 3)$$

**Appendix C. Expressions for the coefficients used in (6.21)**

The coefficients of (6.21) are as follows:

$$\mathcal{L}_0 = DeLe(Le + \chi + Le\chi), \quad (\text{C } 1)$$

$$\mathcal{L}_1 = Le^2(1 + \chi)(BiDe - 1) + 2BiDeLe\chi - \chi(1 + Le), \quad (\text{C } 2)$$

$$\mathcal{L}_2 = Bi\chi(BiDeLe - Le - 2), \quad (\text{C } 3)$$

$$\mathcal{L}_3 = -Bi^2\chi, \quad (\text{C } 4)$$

$$\mathcal{L}_4 = -De, \quad (\text{C } 5)$$

$$\mathcal{L}_5 = 1 + \chi - BiDe. \quad (\text{C } 6)$$

## REFERENCES

- ARAFUNE, K., YAMAMOTO, K. & HIRATA, A. 2001 Interactive thermal and solutal Marangoni convection during compound semiconductor growth in a rectangular open boat. *Int'l J. Heat Mass Transfer* **44** (13), 2405–2411.
- BASSOU, N. & RHARBI, Y. 2009 Role of Bénard-Marangoni instabilities during solvent evaporation in polymer surface corrugations. *Langmuir* **25**, 624–632.
- BATSON, W., CUMMINGS, L. J., SHIROKOFF, D. & KONDIC, L. 2019 Oscillatory thermocapillary instability of a film heated by a thick substrate. *J. Fluid Mech.* **872**, 928–962.
- BÉNARD, H. 1901 Les tourbillons cellulaires dans une nappe de liquide transportant de la chaleur par convection en régime permanent. *Ann. Chim. Phys.* **23**, 62–144.
- BESTEHORN, M. & BORCIA, I. D. 2010 Thin film lubrication dynamics of a binary mixture: Example of an oscillatory instability. *Phys. Fluids* **22** (10), 104102.
- BHATTACHARJEE, J. K. 1994 Marangoni convection in binary liquids. *Phys. Rev. E* **50** (2), 1198–1205.
- BIRD, R. B., ARMSTRONG, R. C. & HASSAGER, O. 1987 *Dynamics of Polymeric Liquids. Vol. 1: Fluid Mechanics*. Wiley.
- BORMASHENKO, E., BALTER, S., POGREB, R., BORMASHENKO, Y., GENDELMAN, O. & AURBACH, D. 2010 On the mechanism of patterning in rapidly evaporated polymer solutions: Is temperature-gradient-driven Marangoni instability responsible for the large-scale patterning? *J. Colloid Interface Sci.* **343**, 602–607.
- CHEN, Z. W., LI, Y. & ZHAN, J. M. 2010 Double-diffusive Marangoni convection in a rectangular cavity: onset of convection. *Phys. Fluids* **22** (3), 034106.
- COLINET, P., LEGROS, J. C. & VELARDE, M. G. 2001 *Nonlinear Dynamics of Surface-Tension-Driven Instabilities*. Wiley.
- CRASTER, R. V. & MATAR, O. K. 2009 Dynamics and stability of thin liquid films. *Rev. Mod. Phys.* **81** (3), 1131–1198.
- D'ALESSIO, S. J. D., PASCAL, J. P., ELLABAN, E. & RUYER-QUIL, C. 2020 Marangoni instabilities associated with heated surfactant-laden falling films. *J. Fluid Mech.* **887**, A20.
- DAUBY, P. C., PARMENTIER, P., LEBON, G. & GRMELA, M. 1993 Coupled buoyancy and thermocapillary convection in a viscoelastic Maxwell fluid. *J. Phys: Condens. Matter* **5** (26), 4343–4352.



- DOUMENC, F., BOECK, T., GUERRIER, B. & ROSSI, M. 2010 Transient Rayleigh–Bénard–Marangoni convection due to evaporation: a linear non-normal stability analysis. *J. Fluid Mech.* **648**, 521–539.
- DOUMENC, F., CHÉNIER, E., TROUETTE, B., BOECK, T., DELCARTE, C., GUERRIER, B. & ROSSI, M. 2013 Free convection in drying binary mixtures: solutal versus thermal instabilities. *Intl J. Heat Mass Transfer* **63**, 336–350.
- FAYZRAKHMANOVA, I. S., SHKLYAEV, S. & NEPOMNYASHCHY, A. A. 2013 Influence of low-frequency vibration on thermocapillary instability in a binary mixture with the Soret effect: long-wave versus short-wave perturbations. *J. Fluid Mech.* **714**, 190–212.
- DE GANS, B. J., KITA, R., WIEGAND, S. & LUETTNER-STRATHMANN, J. 2003 Unusual thermal diffusion in polymer solutions. *Phys. Rev. Lett.* **91** (24), 245501.
- GETACHEW, D. & ROSENBLAT, S. 1985 Thermocapillary instability of a viscoelastic liquid layer. *Acta Mech.* **55** (1–2), 137–149.
- DE GROOT, S. R. & MAZUR, P. 2011 *Non-Equilibrium Thermodynamics*. Dover Publications.
- HERIOT, S. Y. & JONES, R. A. L. 2005 An interfacial instability in a transient wetting layer leads to lateral phase separation in thin spin-cast polymer-blend films. *Nat. Mater.* **4**, 782.
- HIRATA, S. C., DE B. ALVES, L. S., DELENDA, N. & OUARAZI, M. N. 2015 Convective and absolute instabilities in Rayleigh–Bénard–Poiseuille mixed convection for viscoelastic fluids. *J. Fluid Mech.* **765**, 167–210.
- HO, K. L. & CHANG, H. C. 1988 On nonlinear doubly-diffusive marangoni instability. *AIChE J.* **34** (5), 705–722.
- HU, J., HADID, H. B., HENRY, D. & MOJTABI, A. 2008 Linear temporal and spatio-temporal stability analysis of a binary liquid film flowing down an inclined uniformly heated plate. *J. Fluid Mech.* **599**, 269–298.
- JOO, S. W. 1995 Marangoni instabilities in liquid mixtures with Soret effects. *J. Fluid Mech.* **293**, 127–145.
- KELLER, H. B. 2018 *Numerical Methods for Two-Point Boundary-Value Problems*. Dover Publications.
- LEBON, G., PARMENTIER, P., TELLER, O. & DAUBY, P. C. 1994 Bénard–Marangoni instability in a viscoelastic Jeffreys’ fluid layer. *Rheol. Acta* **33** (4), 257–266.
- MAXWELL, J. C. 1867 On the dynamical theory of gases. *Phil. Trans. R. Soc. Lond.* **157** (235), 49–88.
- MCFADDEN, G. B., CORIELL, S. R. & LOTT, P. A. 2010 Onset of convection in two layers of a binary liquid. *J. Fluid Mech.* **647**, 105–124.
- MCTAGGART, C. L. 1983 Convection driven by concentration- and temperature-dependent surface tension. *J. Fluid Mech.* **134** (1), 301–310.
- NEPOMNYASHCHY, A. A. 2001 *Interfacial Phenomena and Convection*. Chapman and Hall/CRC.
- ORON, A., DAVIS, S. H. & BANKOFF, S. G. 1997 Long-scale evolution of thin liquid films. *Rev. Mod. Phys.* **69** (3), 931–980.
- ORON, A. & NEPOMNYASHCHY, A. A. 2004 Long-wavelength thermocapillary instability with the Soret effect. *Phys. Rev. E* **69** (1), 016313.
- PARMENTIER, P., LEBON, G. & REGNIER, V. 2000 Weakly nonlinear analysis of Bénard–Marangoni instability in viscoelastic fluids. *J. Non-Newtonian Fluid Mech.* **89** (1–2), 63–95.
- PEARSON, J. R. A. 1958 On convection cells induced by surface tension. *J. Fluid Mech.* **4**, 489–500.
- PILLAI, D. S. & NARAYANAN, R. 2018 Rayleigh–Taylor stability in an evaporating binary mixture. *J. Fluid Mech.* **848**, R1.
- PODOLNY, A., ORON, A. & NEPOMNYASHCHY, A. A. 2005 Long-wave Marangoni instability in a binary-liquid layer with deformable interface in the presence of Soret effect: linear theory. *Phys. Fluids* **17** (10), 104104.
- RAMKISSOON, H., RAMDATH, G., COMMISSIONG, D. & RAHAMAN, K. 2006 On thermal instabilities in a viscoelastic fluid. *Intl J. Non-Linear. Mech.* **41** (1), 18–25.
- SARMA, R. & MONDAL, P. K. 2018 Marangoni instability in a thin film heated from below: effect of nonmonotonic dependence of surface tension on temperature. *Phys. Rev. E* **97** (4), 043105.
- SARMA, R. & MONDAL, P. K. 2019 Marangoni instability in a heated viscoelastic liquid film: long-wave versus short-wave perturbations. *Phys. Rev. E* **100** (1), 013103.
- SCHATZ, M. F. & NEITZEL, G. P. 2001 Experiments on thermocapillary instabilities. *Annu. Rev. Fluid Mech.* **33** (1), 93–127.

- SHKLYAEV, S., ALABUZHEV, A. A. & KHENNER, M. 2012 Long-wave Marangoni convection in a thin film heated from below. *Phys. Rev. E* **85** (1), 016328.
- SHKLYAEV, S. & NEPOMNYASHCHY, A. A. 2013 Longwave Marangoni convection in a surfactant solution between poorly conducting boundaries. *J. Fluid Mech.* **718**, 428–456.
- SHKLYAEV, S. & NEPOMNYASHCHY, A. A. 2017 *Longwave Instabilities and Patterns in Fluids*. Springer.
- SHKLYAEV, S., NEPOMNYASHCHY, A. A. & ORON, A. 2009 Marangoni convection in a binary liquid layer with Soret effect at small Lewis number: linear stability analysis. *Phys. Fluids* **21** (5), 054101.
- SKARDA, J. R. L., JACQMIN, D. & MCCAUGHAN, F. E. 1998 Exact and approximate solutions to the double-diffusive Marangoni–Bénard problem with cross-diffusive terms. *J. Fluid Mech.* **366**, 109–133.
- TOUSSAINT, G., BODIGUEL, H., DOUMENC, F., GUERRIER, B. & ALLAIN, C. 2008 Experimental characterization of buoyancy- and surface tension-driven convection during the drying of a polymer solution. *Intl J. Heat Mass Transfer* **51**, 4228–4237.
- WÜRGER, A. 2007 Thermophoresis in colloidal suspensions driven by marangoni forces. *Phys. Rev. Lett.* **98** (13), 138301.
- YIANTSIOS, S. G., SERPETSIS, S. K., DOUMENC, F. & GUERRIER, B. 2015 Surface deformation and film corrugation during drying of polymer solutions induced by Marangoni phenomena. *Intl J. Heat Mass Transfer* **89**, 1083–1094.
- ZHANG, M. & MÜLLER-PLATHE, F. 2006 The Soret effect in dilute polymer solutions: influence of chain length, chain stiffness, and solvent quality. *J. Chem. Phys.* **125** (12), 124903.